International Journal of Solids and Structures 168 (2019) 41–57

Contents lists available at ScienceDirect

International Journal of Solids and Structures

journal homepage: www.elsevier.com/locate/ijsolstr

Peridynamic simulation of two-dimensional axisymmetric pull-out tests

Yong Zhang[a], Pizhong Qiao[a,b,*]

[a] State Key Laboratory of Ocean Engineering, School of Naval Architecture, Ocean and Civil Engineering, Shanghai Jiao Tong University, Shanghai 200240, PR China

[b] Department of Civil and Environmental Engineering, Washington State University, Sloan Hall 117, Pullman, WA 99164-2910, USA

ARTICLE INFO

Article history:
Received 5 December 2018
Revised 9 February 2019
Available online 14 March 2019

Keywords:
Pull-out test
Peridynamics
Axisymmetric model
Failure criterion
Contact
Bond-slip behavior

ABSTRACT

In this study, a systematic pull-out simulation scheme in the formwork of two dimensional (2D) axisymmetric domain using peridynamics (PD) is presented. An axisymmetric ordinary state-based peridynamic model is used to model the pull-out deformation just like the axisymmetric stress element in the finite element method (FEM). A failure criterion based on the bond energy density is adopted to predict the interfacial debonding, while a new PD contact model in the 2D axisymmetric domain is proposed to simulate the friction sliding during the pull-out process. The PD pull-out simulation scheme based on the respective 2D axisymmetric model, interfacial failure criterion and contact model is quantitatively validated in comparisons with either the FEM or analytical solutions. The whole process of the pull-out test is simulated using the proposed PD scheme, and the influences of both the interfacial fracture toughness and friction coefficient on the bond-slip behavior are investigated. The developed PD pull-out modeling scheme is capable of effectively simulating the pull-out tests and predicting the bond-slip behavior.

1. Introduction

Pull-out tests are a kind of very important experiments to study the bond-slip behaviors in reinforced structures and composites. For example, the FRP or steel bar pull-out tests from concrete (Baena et al., 2009; Cosenza et al., 1997; Larralde and Silva-Rodriguez, 1993; Torre-Casanova et al., 2013; Zhou and Qiao 2018) were commonly utilized to study the bond behaviors between concrete and bars when using the bars as reinforcement in concrete structures to improve their mechanical resistance. The single fiber pull-out tests (Beglarigale and Yazici, 2015; Cunha et al., 2010; DiFrancia et al., 1996; Takaku and Arridge, 1973) were also adopted to study the interface properties in the fiber reinforced composites. Pull-out tests are widely used at different scales (Baena et al., 2009; Delfolie et al., 1999; Fang et al., 2006; Qian et al., 2000; Shannag et al., 1997; Singh et al., 2004) in applied science and engineering to test models and/or empirically understand the behavior of composite materials and its reinforcement.

The results of a pull-out test typically show three phases (Gao et al., 1988; Zhou et al., 1993) of the bar or fiber displacement: (1) continuous deformation, (2) interfacial debonding, and (3) friction sliding. These three phases are not completely separated from each other during the pull-out test, because the friction sliding usually occurs on the debonding surfaces even when the interface is not yet totally debonded. Therefore, a whole simulation process of the pull-out test is needed to deal with the interfacial crack propagation and friction contact between the debonding surfaces as well as the large relative displacement between the bar/fiber and the matrix. The coupling issues in a pull-out test discussed above make the modeling process quite difficult and challenging.

Researchers have sought for different numerical models to simulate this important type of tests (Banholzer et al., 2005; Chowdhury and Okabe, 2007; Kang et al., 2014; Povirk and Needleman, 1993; Tsai et al., 2005). Among these numerical models of pull-out tests, the finite element method (FEM) usually serves as one of the best computational frameworks. Povirk and Needleman (1993) implemented almost the earliest FEM for fiber pull-out simulation, in which the fiber was assumed to be rigid and the computed region was confined only to the matrix. Li and Mobasher (1998) considered the deformation of both the fiber and matrix, of which a clamping pressure was applied at the outer layer of matrix elements to simulate the effect of matrix shrinkage and the contact elements of zero thickness were used to model contact effect. Beckert and Lauke (1996, 1997) computed the

* Corresponding author at: Department of Engineering Mechanics, Shanghai Jiao Tong University, Shanghai 200240, PR China.
E-mail addresses: qiao@sjtu.edu.cn, qiao@wsu.edu (P. Qiao).

https://doi.org/10.1016/j.ijsolstr.2019.03.014
0020-7683/

evolution of the energy release rate during the pull-out process using FEM. Pochiraju et al. (2001) and Lin et al. (2001) simulated the single fiber push-out test, the corresponding problem to the pull-out test, in the framework of FEM, respectively. In the study by Pochiraju et al. (2001), the convergence problems due to singular global stiffness matrices were encountered in the simulation; while in the simulation by Lin et al. (2001), the contact was only examined between the originally adjacent volumetric elements, and it was thus not adequate to capture the frictional sliding when the fiber was obviously pulled out from the surrounding matrix. Tsai et al. (2003) first performed simulations with simplified interface models, i.e., the fully-bonded and the friction-only interface models, and they later proposed a relatively advanced one which combined the cohesive zone and friction interface models (Tsai et al., 2005). Ellis et al. (2014) simulated the single fiber pull-out response with account of fiber morphology using FEM in three dimensional (3D) domain which was certainly time consuming. Molecular dynamics (MD) was also used to investigate the pull-out behaviors of carbon nanotube from polymer matrix (Chowdhury and Okabe, 2007; Li et al., 2011; Yang et al., 2012). However, MD simulations are usually limited to very small length scales.

Although the simulation of the pull-out problem has been studied for many years, the difficulties in the numerical treatments to the whole pull-out process are still considerable. The mesh, crack and contact problems as well as many parameters involved in the pull-out process all contribute to the difficulties in continuous pull-out modeling. Peridynamics introduced by Silling (2000) may be an alternative framework to deal with the aforementioned issues. Peridynamics (PD) is a new non-local theory of mechanics and numerical methods because it can simulate crack propagation behaviors naturally (Silling and Askari, 2005). The PD has shown excellent capabilities in many complex problems involving damage (Kilic et al., 2009; Xu et al., 2008; Zhang and Qiao, 2018a), cracks (Bobaru and Zhang, 2015; Ha and Bobaru, 2010; Zhang and Qiao, 2018b; Zhou et al., 2016) as well as contact problems (Dubinsky and Elperin, 2015; Littlewood, 2010; Rabczuk and Ren, 2017; Ye et al., 2017). Lu et al. (2018) conducted the PD simulation of anchor bolt pull-out from concrete using the 2D plane stress bond-based PD model. The advantages of PD in fracture analysis and the complexities of the bar or fiber pull-out problems show that there is a need to develop a natural and efficient PD simulation scheme for pull-out simulation.

In this study, the systematic PD pull-out simulation in the 2D axisymmetric domain using ordinary state-based peridynamics (OSBPD) is for the first time presented. The 2D axisymmetric OSBPD model newly proposed by Zhang and Qiao (2018c) is used, and it serves as the axisymmetric stress element in the FEM framework. A failure criterion developed by Zhang and Qiao (2018c) is also adopted for dealing with the interfacial debonding in pull-out. A new PD contact model is developed for the friction sliding in the pull-out simulation. These three individual modeling parts (i.e., the axisymmetric OSBPD model, failure criterion for interfacial debonding, and contact model) form the PD pull-out simulation scheme, and they are used to simulate the whole process of the pull-out test continuously and naturally.

The paper is organized as follows. Section 2 introduces the theoretical backgrounds needed in the present PD modeling, i.e., the axisymmetric OSBPD model, the failure criterion for interfacial debonding, and the PD contact model. Section 3 gives the necessary information about the program implementation of the PD pull-out simulation scheme. Section 4 provides the step-by-step as well as whole quantitative validations in the PD pull-out simulation. In particular, the influence of two key parameters (i.e., the friction coefficient and the interfacial fracture toughness) on the pull-out behavior is investigated in Section 4.

2. Peridynamic modeling

The peridynamic modeling for the pull-out tests in this study consists of three parts, i.e., the axisymmetric ordinary state-based peridynamics (OSBPD) model, the failure criterion for interfacial debonding based on the critical bond energy density, and the PD contact-friction model. They form the whole framework to handle the corresponding issues in pull-out tests, i.e., axisymmetric pull-out deformation, interfacial debonding, and friction sliding.

2.1. Axisymmetric PD model for pull-out deformation

In peridynamics (PD), every material point is connected to other points inside a certain region called “horizon” based on the idea of long range force. The horizon is usually defined to be a sphere in the 3D domain or a disk in the 2D domain centering at the material point with a radius δ, and all the connected points are neighbor points of the central material point. These connections, called peridynamic bonds, are used to generate interactions between the bonded points. The equation of motion can be written as

$$\rho(\mathbf{x})\ddot{\mathbf{u}}(\mathbf{x},t)=\int_H\left(\underline{\mathbf{T}}[\mathbf{x},t]\langle\mathbf{x}'-\mathbf{x}\rangle-\underline{\mathbf{T}}[\mathbf{x}',t]\langle\mathbf{x}-\mathbf{x}'\rangle\right)dV_{\mathbf{x}'}+\mathbf{b}(\mathbf{x},t) \tag{1}$$

where ρ is the density at point $\mathbf{x}$, and $\mathbf{u}$ is the displacement of $\mathbf{x}$ at time t. H is the horizon, and $\mathbf{x}'$ is one of material points bonded to $\mathbf{x}$. $\mathbf{x}'-\mathbf{x}$ is the bond vector which is also written as $\boldsymbol{\xi}$. $dV_{\mathbf{x}'}$ is the infinitesimal volume associated to $\mathbf{x}'$, and it is also denoted as $dV_{\boldsymbol{\xi}}$. $\mathbf{b}$ is the external body force. $\underline{\mathbf{T}}[\mathbf{x},t]$ is the force vector state defined in the state-based theory, and $\underline{\mathbf{T}}[\mathbf{x},t]\langle\mathbf{x}'-\mathbf{x}\rangle$ can be viewed as a mapping from the vector $\mathbf{x}'-\mathbf{x}$ to the certain force vector.

The force vector in OSBPD is parallel to the deformed bond vector $\mathbf{y}'-\mathbf{y}$ or $\underline{\mathbf{Y}}\langle\xi\rangle$, where $\mathbf{y}$ and $\mathbf{y}'$ are the positions of $\mathbf{x}$ and $\mathbf{x}'$ in the deformed configuration, respectively. The force vector in OSBPD can also be expressed as

$$\underline{\mathbf{T}}\langle\xi\rangle=\underline{t}\langle\xi\rangle\frac{\underline{\mathbf{Y}}\langle\xi\rangle}{|\underline{\mathbf{Y}}\langle\xi\rangle|} \tag{2}$$

where $\underline{t}$ is the scalar force state. The scalar force state of OSBPD models in 3D and 2D plane stress/strain conditions was derived by Silling et al. (2007) and Le et al. (2014), respectively. The 2D axisymmetric type of OSBPD model is recently developed by Zhang and Qiao (2018c).

In the 2D axisymmetric PD model, all peridynamic points lie in the half-plane passing through the axis of symmetry. A coordinate r-z is adopted to describe variables of these points. Based on the axisymmetric characteristics, the PD elastic energy density at a point $\mathbf{x}$ in the axisymmetric PD model is written as

$$W(\mathbf{x})=\frac{\lambda'}{2}\left(\Theta^*+\frac{u_r}{r}\right)^2+\frac{\beta}{2}(\underline{\omega e})\bullet\underline{e}+\frac{\gamma}{2}\left(\frac{u_r}{r}\right)^2+\alpha\Theta^*\left(\frac{u_r}{r}\right) \tag{3}$$

where λ', β, γ, α are the PD parameters whose relationships with classical Lamé constants will be given later in Eq. (11). $\underline{\omega}$ is the influence function whose value at a bond vector $\boldsymbol{\xi}$ depends only on the bond length $|\boldsymbol{\xi}|$. $\underline{x}$ is the position scalar state whose value at $\boldsymbol{\xi}$ is the bond length $|\boldsymbol{\xi}|$. $\underline{e}$ is the extension scalar state whose value at $\boldsymbol{\xi}$ is the bond elongation. u_r and r denote the radial displacement and radial coordinate of the concerned material point, respectively. The dot product ($\bullet$) of two PD states is defined by Silling et al. (2007), and it is simply the integration of the regular product over the horizon if two PD states are in scalar states.

The variable Θ^* is defined as

$$\Theta^*=\frac{2\underline{\omega x}\bullet\underline{e}}{q} \tag{4}$$

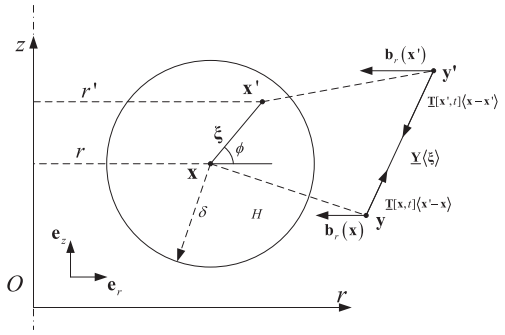

Fig. 1. Axisymmetric ordinary state-based peridynamic model.

where q is the weighted volume, and it is written as

$$q = \underline{\omega x} \bullet \underline{x} = \int_H \underline{\omega}\langle\xi\rangle|\xi|^2 dV_\xi \tag{5}$$

$dV_{\boldsymbol{\xi}}$ is the infinitesimal volume of one neighbor point $\mathbf{x}'$ from the view of the central point $\mathbf{x}$. It is emphasized that the representative volume of one material point is proportional to its radial coordinate in the proposed 2D axisymmetric PD model. Therefore, as seen in Fig. 1, one has

$$dV_\xi = 2\pi r'|\xi|d|\xi|d\phi = 2\pi(r + |\xi|\cos\phi)|\xi|d|\xi|d\phi \tag{6}$$

And the weighted volume is thus calculated as

$$\begin{aligned} q &= 2\pi\int_0^\delta\int_0^{2\pi}\underline{\omega}\langle\xi\rangle|\xi|^2(r+|\xi|\cos\phi)|\xi|d|\xi|d\phi \\ &= (2\pi)(2\pi r)\int_0^\delta \underline{\omega}\langle\xi\rangle|\xi|^3 d|\xi| \end{aligned} \tag{7}$$

which indicates that the weighted volume in the 2D axisymmetric PD model is not a uniform value even though all points share the same δ.

As shown in Eq. (3), the PD elastic energy density in the 2D axisymmetric PD model is a variable depending not only on the extension scalar state $\underline{e}$, but also on the radial displacement u_r. In the 2D axisymmetric PD model, an extra body force $\mathbf{b}_r$ perpendicular to the symmetric axis is needed by the equilibrium of axisymmetric body, and it is calculated by the derivative of W with respect to u_r in Eq. (8). As shown in Fig. 1, for the unification of the notation, an extra body force $\mathbf{b}_r$ is written as

$$\mathbf{b}_r = b_r(-\mathbf{e}_r) \tag{8}$$

where $\mathbf{e}_r$ is the unit vector in the same direction as the r-axis. According to the derivative of W with respect to $\underline{e}$ and u_r, one can obtain

$$\underline{t} = \left[\lambda'\Theta^* + \left(\lambda'+\alpha\right)\frac{u_r}{r}\right]\frac{2\underline{\omega x}}{q} + \beta\underline{\omega e} \tag{9}$$

and

$$b_r = \frac{1}{r}\left[\left(\lambda'+\alpha\right)\Theta^* + \left(\lambda'+\gamma\right)\frac{u_r}{r}\right] \tag{10}$$

The PD parameters in Eqs. (3), (9) and (10) are calculated as

$$\begin{aligned} \lambda' &= \lambda - \mu \\ \beta &= \frac{8\mu}{q} \\ \gamma &= 3\mu \\ \alpha &= \mu \end{aligned} \tag{11}$$

by equalizing W to the corresponding strain energy density in the classical theory. λ and μ are the Lamé constants. More details about the derivation can be found in Zhang and Qiao (2018c). The internal forces given by Eqs. (9)-(11) and non-uniform volume distribution described by Eqs. (6) and (7) compose the 2D axisymmetric PD model which is used for the axisymmetric pull-out deformation in the 2D domain.

2.2. Failure criterion for interfacial debonding

In peridynamic models, the formation of damages and cracks is based on the accumulation of bond breakage. It allows bonds to break irreversibly when a certain failure criterion is satisfied. The interaction or the force vector associated with that bond is eliminated from the calculation of the motion equation once the bond is broken. The local damage at a point is computed as the ratio of the number of the broken bonds to the total number of all the bonds owned by this point. A failure criterion based on the bond energy density (Foster et al., 2011) is adopted in the 2D axisymmetric PD model for interfacial debonding prediction. It is assumed that there is a critical energy density $\bar{w}_c$ associated with a certain bond. The bond will be broken if the energy density $\bar{w}$ contained in the bond exceeds the critical value $\bar{w}_c$. The calculation of $\bar{w}$ is performed by

$$\bar{w} = \int_0^t \left(\underline{\mathbf{T}}[\mathbf{x},t]\langle\mathbf{x}'-\mathbf{x}\rangle - \underline{\mathbf{T}}[\mathbf{x}',t]\langle\mathbf{x}-\mathbf{x}'\rangle\right)\cdot\underline{\dot{\mathbf{Y}}}[\mathbf{x},t]\langle\mathbf{x}'-\mathbf{x}\rangle dt \tag{12}$$

where t indicates the time and $\underline{\dot{\mathbf{Y}}}$ is the time derivative of the deformation state. The critical value $\bar{w}_c$ corresponding to $\bar{w}$ in the 2D axisymmetric PD model is determined to be (Zhang and Qiao, 2018c)

$$\bar{w}_c = \frac{3G_c}{8\pi\delta^3}\left(\frac{1}{r_{\mathbf{x}}} + \frac{1}{r_{\mathbf{x}'}}\right) \tag{13}$$

where G_c is the critical energy release rate (fracture toughness) in classical fracture mechanics. $r_{\mathbf{x}}$ and $r_{\mathbf{x}'}$ are the radial coordinates of the central and neighbor points connected by the concerned bond.

If the dual force density property (Bobaru et al., 2016; Ren et al., 2017; Silling et al., 2007; Silling and Lehoucq, 2010) of the state-based peridynamics is considered, the concerned bond between $\mathbf{x}$ and $\mathbf{x}'$ will be distinguished into the bond $\mathbf{x}'-\mathbf{x}$ originating at $\mathbf{x}$ and another one $\mathbf{x}-\mathbf{x}'$ originating at $\mathbf{x}'$. In this situation, the bond energy density in the view of $\mathbf{x}$ is redefined as

$$w = \int_0^t \underline{\mathbf{T}}[\mathbf{x},t]\langle\mathbf{x}'-\mathbf{x}\rangle\cdot\underline{\dot{\mathbf{Y}}}[\mathbf{x},t]\langle\mathbf{x}'-\mathbf{x}\rangle dt \tag{14}$$

and the critical value w_c corresponding to w is separated from $\bar{w}_c$ as

$$w_c = \frac{3G_c}{8\pi\delta^3 r_{\mathbf{x}}} \tag{15}$$

The critical bond energy density criterion presented above can be used to judge the breakage of the interfacial peridynamic bonds in the pull-out simulation and thus the associated interfacial debonding when the critical energy release rate of interface bond (interfacial fracture toughness) is given as an input parameter.

2.3. Peridynamic contact model for friction sliding

The shrinkage of the matrix induces a contact between debonding surfaces (Penn et al., 1989), and the friction sliding due to the interface contact cannot be neglected in the pull-out simulation. Thus, a PD contact model is needed in the PD pull-out simulation.

Contact in peridynamics involves material points that are disconnected at the onset of a simulation or those that become disconnected as a result of bond breakage. As stated in the short-range force approach (Littlewood, 2015; Silling and Askari, 2005) which is the most common approach or framework to model contact in PD, the contact interaction can be generated between a pair of material points only when these two points are disconnected

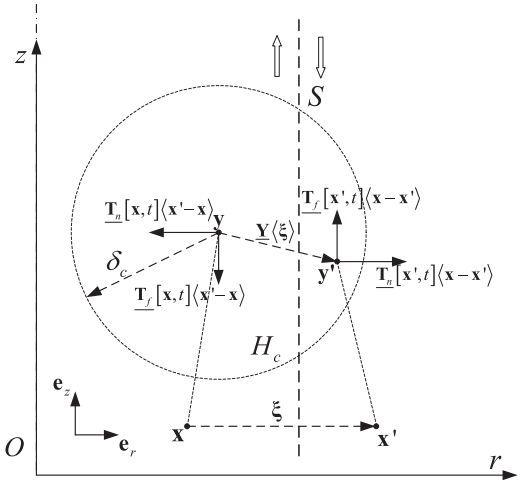

Fig. 2. A peridynamic contact model in the axisymmetric 2D domain.

and close enough. Therefore, as shown in Fig. 2, a contact interaction is established between two points $\mathbf{x}$ and $\mathbf{x}'$, if there is no intact material bond between them and the distance between these two points is smaller than the cut-off distance δ_c. In this study, δ_c is called the contact horizon which will be utilized to determine whether contact interactions between two points should be established.

As also shown in Fig. 2, S is the sliding interface after interfacial debonding. The material points $\mathbf{x}$ and $\mathbf{x}'$ on both sides of the interface move to $\mathbf{y}$ and $\mathbf{y}'$, respectively. The vector $\boldsymbol{\xi}=\mathbf{x}'-\mathbf{x}$ is used for convenience, but the material bond between these two points is disconnected because of either the pre-existing or the newly formed interfacial crack. In the proposed PD contact model, a normal contact force state $\underline{\mathbf{T}}_n$ and a friction force state $\underline{\mathbf{T}}_f$ are defined. When the contact forces are taken into consideration, the motion equation of a point given by Eq. (1) is rewritten as

$$\rho(\mathbf{x})\ddot{\mathbf{u}}(\mathbf{x},t)=\int_H\left(\underline{\mathbf{T}}[\mathbf{x},t]\langle\xi\rangle-\underline{\mathbf{T}}[\mathbf{x}',t]\langle-\xi\rangle\right)dV_{\mathbf{x}'}+\mathbf{b}(\mathbf{x},t)+\int_{H_c}\left(\underline{\mathbf{T}}_n[\mathbf{x},t]\langle\xi\rangle-\underline{\mathbf{T}}_n[\mathbf{x}',t]\langle-\xi\rangle+\underline{\mathbf{T}}_f[\mathbf{x},t]\langle\xi\rangle-\underline{\mathbf{T}}_f[\mathbf{x}',t]\langle-\xi\rangle\right)dV_{\mathbf{x}'} \tag{16}$$

Considering the contact force distribution along the sliding interface, these two force states are written as

$$\underline{\mathbf{T}}_n\langle\xi\rangle=-\underline{t}_n\langle\xi\rangle\mathrm{sgn}(\underline{\mathbf{Y}}\langle\xi\rangle\cdot\mathbf{e}_r)\mathbf{e}_r \tag{17}$$

and

$$\underline{\mathbf{T}}_f\langle\xi\rangle=\underline{t}_f\langle\xi\rangle\mathrm{sgn}\left(\frac{\partial}{\partial t}(\underline{\mathbf{Y}}\langle\xi\rangle\cdot\mathbf{e}_z)\right)\mathbf{e}_z \tag{18}$$

where $\underline{t}_n$ and $\underline{t}_f$ are the corresponding scalar force states. $\mathbf{e}_z$ and $\mathbf{e}_r$ are the unit vectors along the z-axis and r-axis, respectively. For simplification, only the kinetic friction is considered in this model as indicated by Eq. (18)

The Coulomb's friction law is adopted to establish the relationship between the normal contact force and the friction force as

$$\underline{t}_f\langle\xi\rangle=f\underline{t}_n\langle\xi\rangle \tag{19}$$

where f is the coefficient of kinetic friction (Popov, 2010).

Assuming that the normal contact pressure on the debonding surfaces is p_c, the normal contact force state must be determined to recover the normal contact pressure. Since the normal contact pressure p_c has a dimension of force per unit area (N/m^2) and $\underline{t}_n\langle\xi\rangle$ has a dimension of force per unit volume squared (N/m^6), they have the same relationship as that shown by Eq. (15) between G_c (J/m^2) and w_c (J/m^6). Replacing the material horizon δ and the radial coordinate $r_{\mathbf{x}}$ of the initial position $\mathbf{x}$ with the contact horizon δ_c and the radial coordinate $r_{\mathbf{y}}$ of the current position $\mathbf{y}$, one has

$$\underline{t}_n\langle\xi\rangle=\begin{cases}\frac{3p_c}{8\pi\delta_c^3 r_{\mathbf{y}}} & \text{if } |\underline{\mathbf{Y}}\langle\xi\rangle|<\delta_c \text{ and } \xi \text{ is disconected}\\ 0 & \text{otherwise}\end{cases} \tag{20}$$

When $\boldsymbol{\xi}$ is disconnected, there is no intact material bond between material points $\mathbf{x}$ and $\mathbf{x}'$.

The normal contact pressure p_c is evaluated as

$$p_c=E_c\left(\frac{|\underline{\mathbf{X}}\langle\xi\rangle\cdot\mathbf{e}_r|-|\underline{\mathbf{Y}}\langle\xi\rangle\cdot\mathbf{e}_r|}{|\underline{\mathbf{X}}\langle\xi\rangle\cdot\mathbf{e}_r|}\right) \tag{21}$$

When the two points get close to each other in the radial direction, $|\underline{\mathbf{X}}\langle\xi\rangle\cdot\mathbf{e}_r|$ is larger than $|\underline{\mathbf{Y}}\langle\xi\rangle\cdot\mathbf{e}_r|$. E_c is the contact stiffness in the proposed 2D axisymmetric PD contact model, and it is evaluated by

$$\frac{1}{E_c}=\frac{1}{E_1}+\frac{1}{E_2} \tag{22}$$

where E_1 and E_2 are the elastic moduli of the two contact bodies on both sides of the interface. Eq. (22) is used in consideration of the Hertzian contact stiffness (Popov, 2010) in the classical theory. The Poisson's ratios of the contact bodies are not taken into account because the normal contact is assumed to be only relevant to the radial deformation.

3. Program implementation

A computational program is implemented to integrate the three modeling parts (i.e., 2D axisymmetric OSBPD model, failure criterion for interfacial debonding, and contact model for frictional sliding) in Section 2 into one whole for the systematic PD pull-out simulation. The main steps of the PD modeling software and the important numerical treatments used in this study are introduced as follows.

3.1. Fundamental peridynamic program framework

The concerned region in PD can be discretized into nodes with known volumes in the reference configuration. The discretized form of the motion equation, Eq. (16), is written as

$$\rho\ddot{\mathbf{u}}(\mathbf{x}_i,t)=\sum_{j=1}^{k}\left(\underline{\mathbf{T}}[\mathbf{x}_i,t]\langle\xi_i\rangle-\underline{\mathbf{T}}[\mathbf{x}_j,t]\langle-\xi_i\rangle\right)V_j+\mathbf{b}(\mathbf{x}_i,t)+\sum_{j_c=1}^{k_c}\left(\underline{\mathbf{T}}_n[\mathbf{x}_i,t]\langle\xi_i\rangle-\underline{\mathbf{T}}_n[\mathbf{x}_{j_c},t]\langle-\xi_i\rangle+\underline{\mathbf{T}}_f[\mathbf{x}_i,t]\langle\xi_i\rangle-\underline{\mathbf{T}}_f[\mathbf{x}_{j_c},t]\langle-\xi_i\rangle\right)V_{j_c}\ \forall i=1,2,\ldots,N \tag{23}$$

where $\mathbf{x}_i$ represents a discrete material node, $\mathbf{x}_j$ represents a neighbor node of $\mathbf{x}_i$, and k is the total number of neighbor nodes of $\mathbf{x}_i$. Similarly, $\mathbf{x}_{j_c}$ is the contact node of $\mathbf{x}_i$, and k_c is the total number of contact nodes of $\mathbf{x}_i$. N is the total number of nodes of the concerned region.

Explicit time integration (Silling and Askari, 2005) has been commonly used to obtain the value of displacement, velocity and acceleration of PD particles. In the explicit time integration for PD, the kinetic energy is difficult to be eliminated from the system. Therefore, the normal explicit scheme is usually used in dynamic peridynamic simulations, and it is not suitable for quasi-static ones. A very low loading rate may improve the situation, but it needs a lot of time steps, thus resulting in a heavy time cost.

In this study, the quasi-static pull-out is simulated using the adaptive dynamic relaxation (ADR) method as proposed by

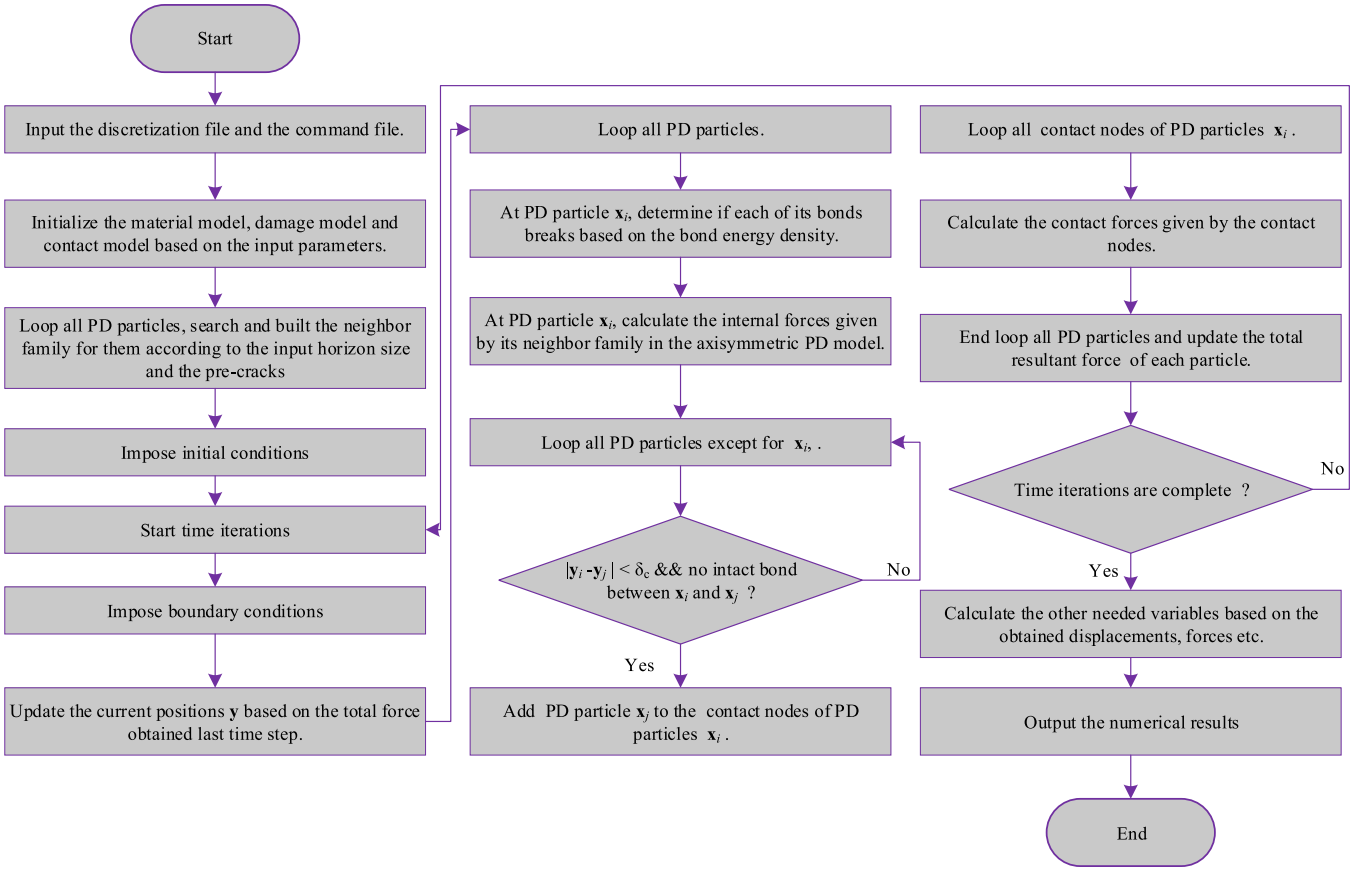

Fig. 3. The flowchart of the PD program for the pull-out simulation.

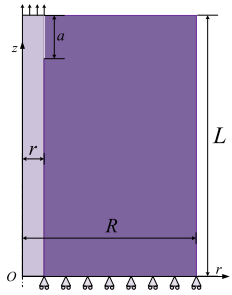

Fig. 4. The geometry and boundary conditions of the bar-matrix system for pull-out deformation.

Kilic and Madenci (2010) because of its feasibility for the quasi-static PD solutions. Replacing the normal density by the fictitious one and introducing the damping coefficients, Eq. (23) can be re-written as

$$\mathbf{\Lambda}\ddot{\mathbf{U}}(\mathbf{X},t) + c\mathbf{\Lambda}\dot{\mathbf{U}}(\mathbf{X},t) = \mathbf{F}\left(\mathbf{U},\mathbf{U}',\mathbf{X},\mathbf{X}'\right) \tag{24}$$

where $\mathbf{\Lambda}$ is the fictitious diagonal density matrix and c is the adaptively-varying damping coefficients. $\mathbf{X}$ and $\mathbf{U}$ represent the positions and displacements of the collocation points, respectively. $\mathbf{F}$ is the resultant force of the collocation points. The iteration program can be written as

$$\dot{\mathbf{U}}^{n+1/2} = [(2 - c^n\Delta t)\dot{\mathbf{U}}^{n-1/2} + 2\Delta t\mathbf{\Lambda}^{-1}\mathbf{F}^n]/(2 + c^n\Delta t) \tag{25}$$

$$\mathbf{U}^{n+1} = \mathbf{U}^n + \Delta t\dot{\mathbf{U}}^{n+1/2} \tag{26}$$

$$c^{n+1} = 2\sqrt{\frac{\left(\mathbf{U}^{n+1}\right)^T\left[\left(\mathbf{F}^n - \mathbf{F}^{n+1}\right)\mathbf{\Lambda}^{-1}/\left(\Delta t\dot{\mathbf{U}}^{n+1/2}\right)\right]\mathbf{U}^{n+1}}{\left[\left(\mathbf{U}^{n+1}\right)^T\mathbf{U}^{n+1}\right]}} \tag{27}$$

where n indicates the nth iteration. Due to the unknown velocity field at $t^{-1/2}$, the integration can be started from $n=1$ by using

$$\dot{\mathbf{U}}^{1/2} = \Delta t\mathbf{\Lambda}^{-1}\mathbf{F}^0/2 \tag{28}$$

$$c^1 = 0 \tag{29}$$

The damping coefficient is set to zero whenever zero velocity or zero displacement is encountered so that the division by zero can be avoided. The time step can be chosen as 1 for the sake of convenience (Kilic and Madenci, 2010). The detailed calculation of the fictitious diagonal density matrix $\mathbf{\Lambda}$ for the 2D axisymmetric PD model can be found in Zhang and Qiao (2018c).

A flowchart of the PD program is shown in Fig. 3. The displacements of the PD particles are updated in each time iteration according to Eqs. (25)-(27). The breakage of the bond is determined according to the failure criterion in Section 2.2, while the internal forces are calculated by the 2D axisymmetric PD model in Section 2.1. The volume modification scheme considered in Le et al. (2014) is adopted in the PD model to reduce the discretization effect in discrete PD numerical implementations. The contact forces between some PD particles are calculated by the PD contact model in Section 2.3.

As exhibited in Fig. 3, the material bonds or the neighbor family of each PD particle are built on the initial configuration by just one search before the time iterations, but the contact nodes of a

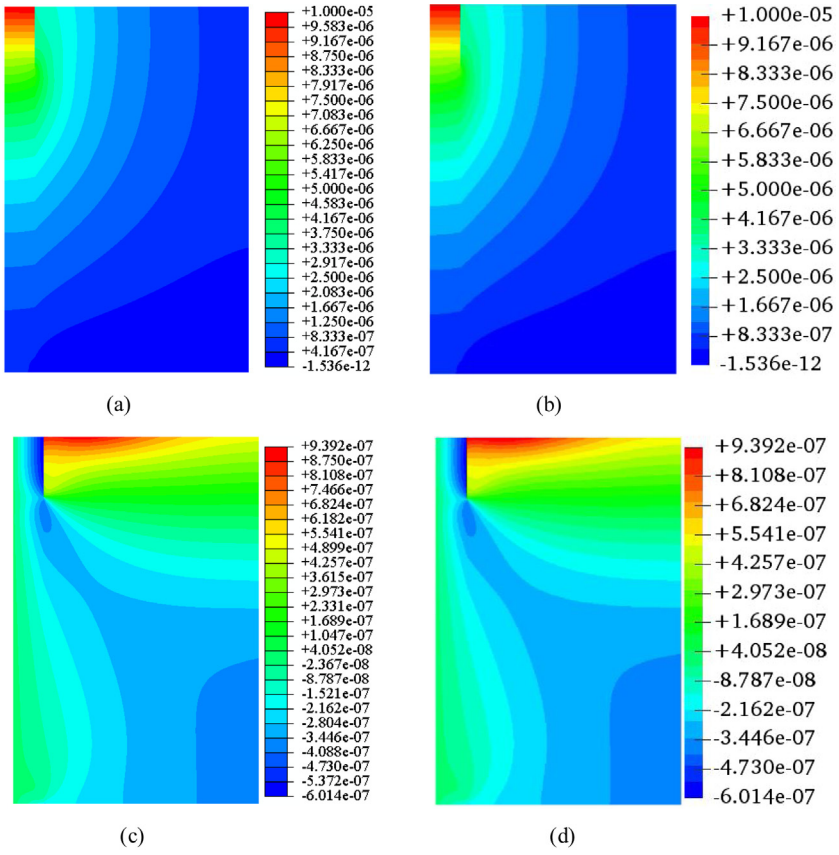

Fig. 5. Displacement fields in pull-out deformation: (a) the z component by FEM (m), (b) the z component by PD (m); (c) the r component (m) by FEM, and (d) the r component (m) by PD.

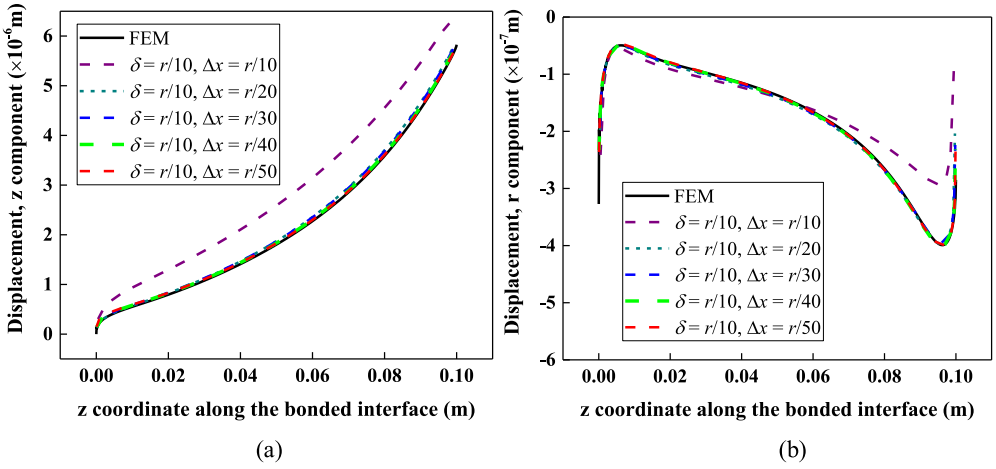

Fig. 6. Displacement components with different Δx and a fixed δ: (a) z component, and (b) r component, along the bonded interface between the bar and the matrix.

PD particle are searched instantaneously on the current configuration, which will increase the computational cost. The special treatments adopted in this study to reduce computational time and related costs in PD contact implementation are described in the next section.

3.2. Special treatments for time-cost saving

The contact model, including the search of the contact pairs as well as the calculation of contact forces, is applied to the whole PD discretization region in the program as shown in Fig. 3. However, for the pull-out simulation in this study, contact only occurs near the interface between the matrix and the bar or the fiber. Therefore, a contact region is pre-defined along the interface for the contact model. The contact region can be set as small as possible, but at least it covers all the PD particles where contact may occur. A pre-defined contact region can limit the contact search and computation within this sub-region instead of the whole peridynamic discretization body, and it can thus reduce the contact computational time cost.

As also shown in Fig. 3, one can search the contact nodes for the particle $\mathbf{x}_i$ in every time iteration. Because the deformation configuration does not change very much in time, there is no need to update the contact neighbors of $\mathbf{x}_i$ in the quasi-static pull-out simulation every single time step. Hence, an alternative strategy is adopted, in which the contact pairs are searched and updated ev-

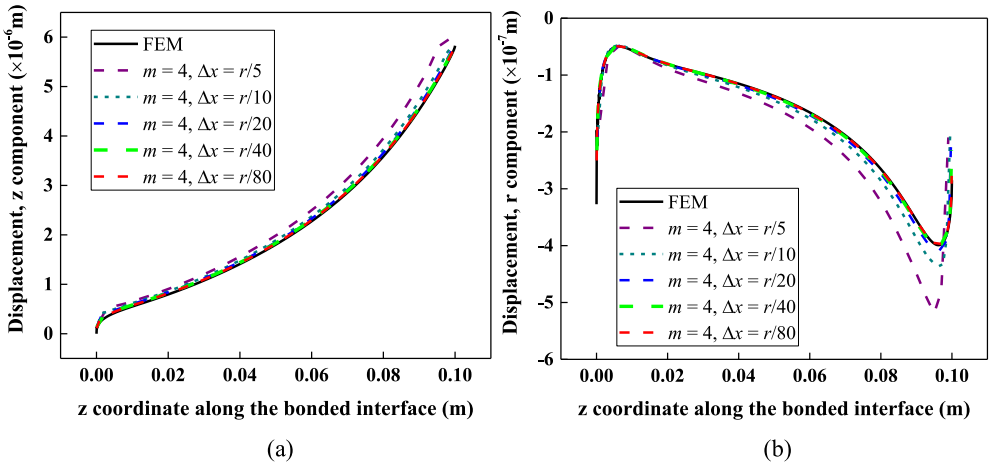

Fig. 7. Displacement components with different Δx and a fixed m: (a) z component, and (b) r component, along the bonded interface between the bar and the matrix.

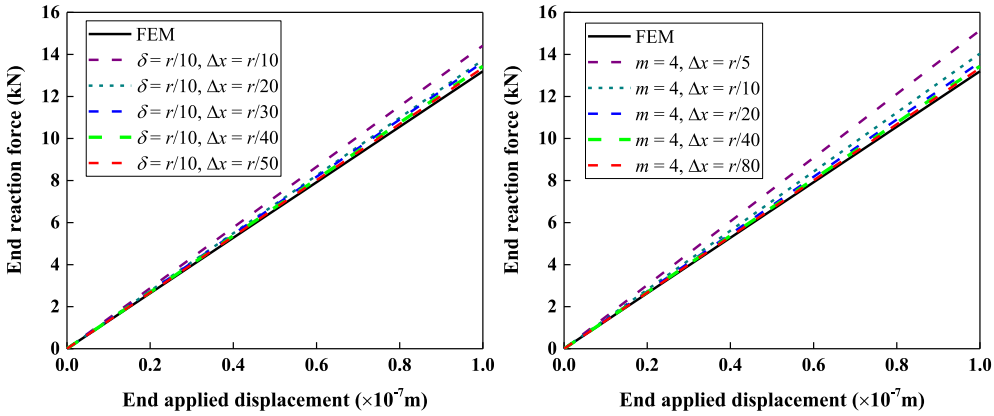

Fig. 8. Force-displacement behaviors in pull-out deformation of different kinds of discretization: (a) m-convergence, and (b) δ-convergence.

Table 1
Material properties of the bar-matrix system.

Bar		Matrix	
Young's modulus E (GPa)	Poisson's ratio ν	Young's modulus E (GPa)	Poisson's ratio ν
210	0.3	40	0.2

ery C_n-time ($C_n > 1$) steps rather than every one time step. The contact neighbors of $\mathbf{x}_i$ are held before next updating, but the contact forces are still calculated every time step based on the current particle positions and contact relationships.

The C++ programming language is used for the implementation of the program, and parallel computing is enabled by referring to Peridigm (Parks et al., 2012) because this open source PD code supplies an excellent parallel computing framework for the mesh-free type of PD solvers. All simulations are run on a work station with a 20-core Intel CPU.

4. Numerical results

Again, the proposed pull-out simulation scheme consists of three aforementioned component models: an axisymmetric PD model for pull-out deformation, a bond failure criterion for interfacial debonding, and a PD contact model for frictional sliding. The verifications for the pull-out simulation scheme are demonstrated step by step based on the validations of these three models successively in Sections 4.1–4.3. In Sections 4.1 and 4.2, the contact on the interface is not considered, and the focus is concentrated in the validation of the 2D axisymmetric PD model and the bond failure criterion. Eventually, in Section 4.3, the bonding of the interface is turned off to verify only the contact model. The whole pull-out process simulation is finally presented in Section 4.4 where both the interfacial bonding/debonding and contact are taken into consideration.

4.1. Axisymmetric pull-out deformation

A bar/fiber-matrix system will experience continuous deformation under the pull-out load before any failure occurs. As shown in Fig. 4, a bar is embedded in the matrix, and both the bar (or fiber) and matrix are considered as cylinders. An axial displacement $u_z = 0.01$ mm is applied to the top end of the bar, and an axial displacement constraint $u_z = 0$ is applied to the bottom of the matrix. The boundary regions are chosen as the outermost layers of particles in the PD numerical implementation. The length of the bar is $L = 120$ mm which is equal to the height of the matrix. A pre-existing ring crack with length $a = 20$ mm is inserted into the peridynamic discretization. The radii of the bar and the matrix are $r = 10$ mm and $R = 80$ mm, respectively.

The material properties of the bar and matrix used in this study are the same as the ones used by Gao et al. (1988), and they are listed in Table 1. The interface between the bar and the matrix is assumed to be perfectly bonded in this section. It is worth

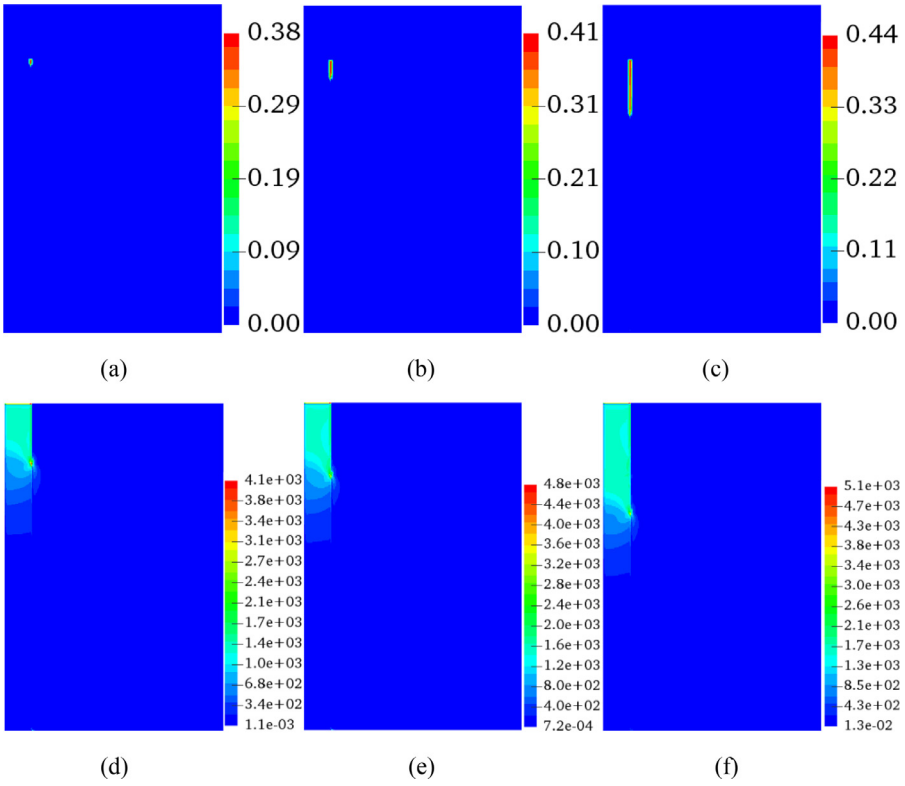

Fig. 9. Local damage at (a) $u = 5.6 \times 10^{-6}$ m, (b) $u = 6.4 \times 10^{-6}$ m, (c) $u = 8.0 \times 10^{-6}$ m, and elastic energy density at (d) $u = 5.6 \times 10^{-6}$ m, (e) $u = 6.4 \times 10^{-6}$ m, (f) $u = 8.0 \times 10^{-6}$ m.

mentioning that the dual force density (Silling and Lehoucq, 2010) defined in the state-based peridynamics can model the interface accounting for different material properties on both sides. Both the theoretical and numerical details of the material interface can be found in the work by Ren et al. (2017).

The axial and radial displacement fields of the pull-out system are compared between the FEM and PD. The FEM results are obtained by ABAQUS using the axisymmetric stress element with the size of 0.1 mm × 0.1 mm. The PD results are first obtained using the horizon radius $\delta = r/10$ and the node size $\Delta x = r/40$. The displacement fields obtained by the FEM and PD are shown and compared in Fig. 5. The same color range is used for both the peridynamic and FEM results in all the comparisons. The color ranges are produced automatically by ABAQUS, and it is set to be the same values in ParaView to post-process the PD results.

As shown in Fig. 5, the numerical results obtained by the 2D axisymmetric PD model agree very well with those by the FEM. The accuracy of the axisymmetric PD model in the pull-out simulation is thus verified even the bi-material and interface exist.

The discretization in PD are defined by the node size Δx, the horizon radius δ, and the ratio $m = \delta/\Delta x$, where two of them are independent. The detailed convergence behaviors of the 2D axisymmetric PD model are previously discussed by Zhang and Qiao (2018c). Both m-convergence and δ-convergence study (Bobaru et al., 2009) are hereby performed to show the influence of the discretization on the PD pull-out deformation results. The radius r of the bar is taken as the characteristic length in different kinds of PD discretization. In m-convergence, δ is fixed as $r/10$ while Δx ranges from $r/10$ to $r/50$, which corresponds to m ranging from 1 to 5. In δ-convergence, the m value is fixed as 4 and Δx ranges from $r/5$ to $r/80$ or δ from $0.8r$ to $0.05r$ in other words.

The results of the m-convergence and the δ-convergence are shown in Figs. 6 and 7, respectively, where Figs. 6(a) and 7(a) are for the axial displacement (the z component) and Figs. 6(b) and 7(b) are for the radial displacement (the r component). As shown in Figs. 6 and 7, the predicted displacement components along the bonded interface by the PD model are in good agreements with the FEM curves for most of discretization cases above. It is found that the coarsest node size Δx in both m-convergence and δ-convergence will cause the most considerable deviations. The relative errors between the PD results and the FEM ones decrease slowly when the node size Δx is small enough in the convergence study.

The pull-out force-displacement responses in the continuous pull-out deformation stage are also investigated in the convergence study. The pull-out stiffness is defined as the ratio of the end reaction force to the end applied displacement. As shown in Fig. 8, the pull-out system is stiffer if the PD nodes are coarser in both the m-convergence and δ-convergence study.

4.2. Interfacial crack initiation and debonding

The critical bond energy density failure criterion presented in Section 2.2 is now used for the interfacial debonding in the pull-out simulation. The critical bond energy density of bonds across the interface are calculated by Eq. (15) using the critical energy release rate of interface or the interfacial fracture toughness G_{ic} (Zhou et al., 1992). The value $G_{ic} = 6$ J/m^2 used in Gao et al. (1988) is also adopted here. It is assumed that the critical energy release rate of interface (or interfacial fracture toughness) G_{ic} is much smaller than those of the matrix and the bar, resulting in a weak bonding interface. The geometry and the material properties of the pull-out system here are the same as those in Section 4.1. The applied end displacement is denoted as u, and its increment is set as 2×10^{-10} m every time step in the ADR method. The final end displacement u is up to 8×10^{-6} m.

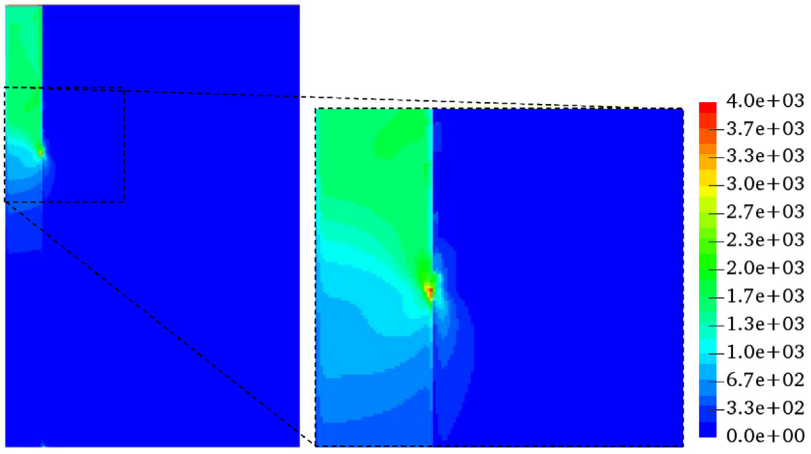

Fig. 10. Zoom-in view of the elastic energy density at $u = 8.0 \times 10^{-6}$ m.

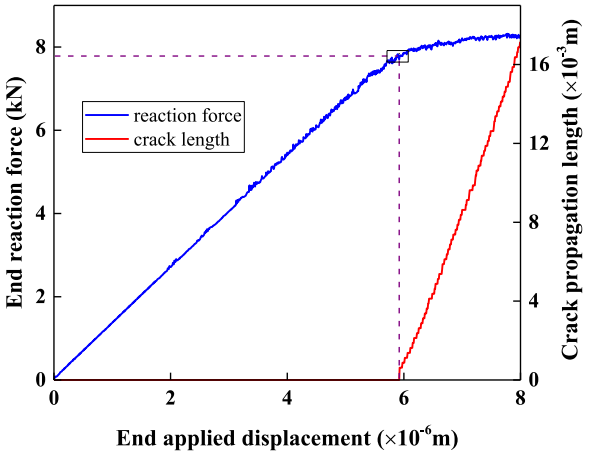

Fig. 11. Critical displacement and force obtained in PD when the crack propagation length is larger than zero.

The interfacial crack initiation and debonding process is first obtained by PD using the discretization of $\delta = r/10$ and $\Delta x = r/40$. The local damage and the elastic energy density during the debonding process are plotted in Fig. 9.

The crack path is indicated by the local damage value. The crack is initiated at the bottom of the pre-crack as shown in Fig. 9(a). It then propagates along the interface as the end pull-out displacement increases. The elastic energy density in Fig. 9(f) is specially plotted in Fig. 10 with a zoom-in view. As seen in Figs. 9(d)-(f) and 10, the elastic energy density concentrating in the newly-formed crack tip leads to further interfacial debonding.

The proposed failure criterion is validated quantitatively by the comparisons of the critical end applied displacements and the critical end reaction forces for interfacial debonding obtained by PD and FEM. As shown in Fig. 11, the critical pull-out displacement and force in PD are determined to be the values in the force-displacement curve when the crack propagation length is larger than zero.

The PD critical values are compared with the FEM results which are obtained by the Virtual Crack Closure Technique (VCCT). The crack propagation length in PD is calculated by monitoring the position of the crack tip where the local damage value exceeds a certain damage value. The computed local damage values near the crack tip or the crack plane is dependent on the chosen m ($\delta/\Delta x$) values. In this study, the damage values indicating the crack tip are prescribed as 0.21, 0.26, 0.37, 0.4 and 0.41 in the cases $m = 1$, 2, 3, 4 and 5 considering that the corresponding maximum computed damage values near crack surfaces are 0.25, 0.3, 0.41, 0.44, and 0.45, respectively. In VCCT, a simple criterion for mix-mode fracture or interfacial debonding considering the absence of additional parameters in some complex fracture criteria, (e.g., the Power Law (Camanho et al., 2003; Wu and Reuter Jr, 1965) and the BK Law (Benzeggagh and Kenane, 1996)) is

$$G_I + G_{II} \geq G_{ic} \tag{30}$$

The predictions of the critical displacement and critical force by the VCCT of FEM are indicated by the black dash lines shown in Figs. 12 and 13.

As shown in Fig. 12, the PD models are computed with $m = 1$, 2, 3, 4, 5 and a fixed value of $\delta = 0.1r$. The PD results in cases of $m > 3$ are quite consistent with the FEM results. The relative errors of the critical displacement between FEM and PD of $m = 4$ and 5 are 1.98% and 1.8%, respectively; while they are 2.4% and 2.2%, respectively, for the critical force. The largest deviation of both the critical displacement and critical force are caused by the smallest m value (i.e., $m = 1$). In Fig. 13, the PD models are computed with $\delta = 0.1r$, $0.2r$, $0.4r$, $0.8r$ and a fixed value of $m = 4$. The PD results agree well with the FEM ones when $\delta < 0.4r$. The relative errors of the critical displacement between FEM and PD of $\delta = 0.1r$ and $0.2r$ are 1.98% and 2.2%, respectively; while they are 2.4% and 6.0%, respectively, for the critical force. Also, as expected, the largest δ value (i.e., $\delta = 0.8r$) results in the largest deviation.

The results above are computed on the geometry where the pre-crack length is $a = 20$ mm and the radius of the bar is $r = 10$ mm. To further investigate the performance of the failure criterion on different geometries, the critical pull-out forces are computed versus different pre-crack lengths at a fixed bar radius $r = 10$ mm, and the critical pull-out stresses are obtained for different bar radii at a fixed pre-crack length $a = 40$ mm.

The critical debonding force in the model given by Stang and Shah (1986) is expressed as

$$P_c = 2\pi r^2 \left(\frac{E_f G_{ic}}{r} \right)^{1/2} \tag{31}$$

where E_f is the elastic modulus of the bar or the fiber. As an improvement, the model developed by Gao et al. (1988) is given as

$$P_c = 2\pi r^2 \left[\frac{E_f G_{ic}(1+\eta)}{r(1-2k\nu_f)} \right]^{1/2} \tag{32}$$

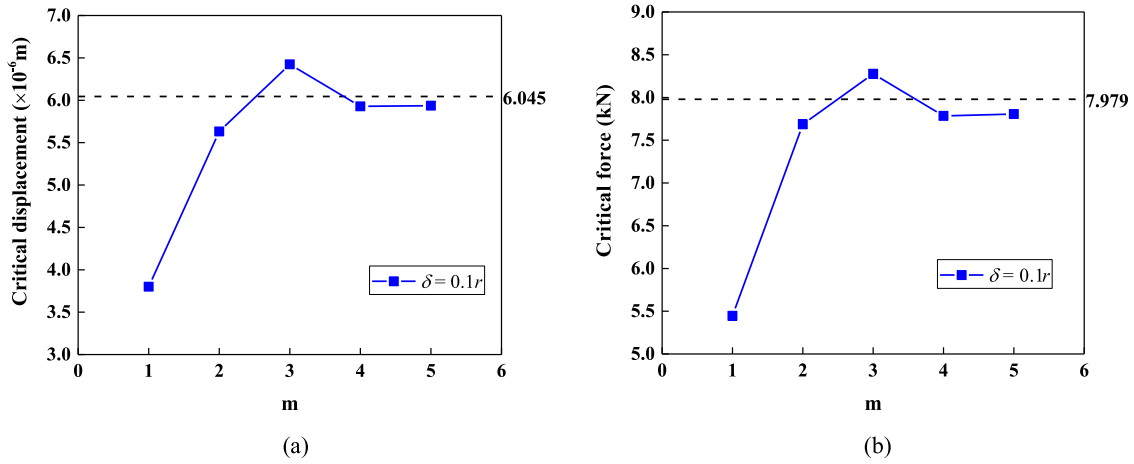

Fig. 12. Critical PD values with different m and a fixed δ (note: the constant lines/values are obtained by FEM): (a) critical displacement, and (b) critical force.

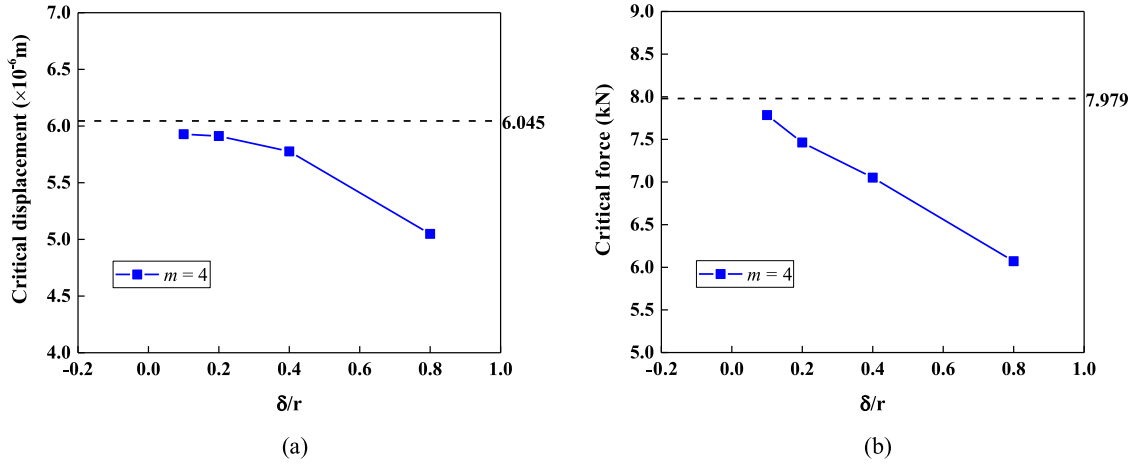

Fig. 13. Critical PD values with different δ and a fixed m (note: the constant lines/values are obtained by FEM): (a) critical displacement, and (b) critical force.

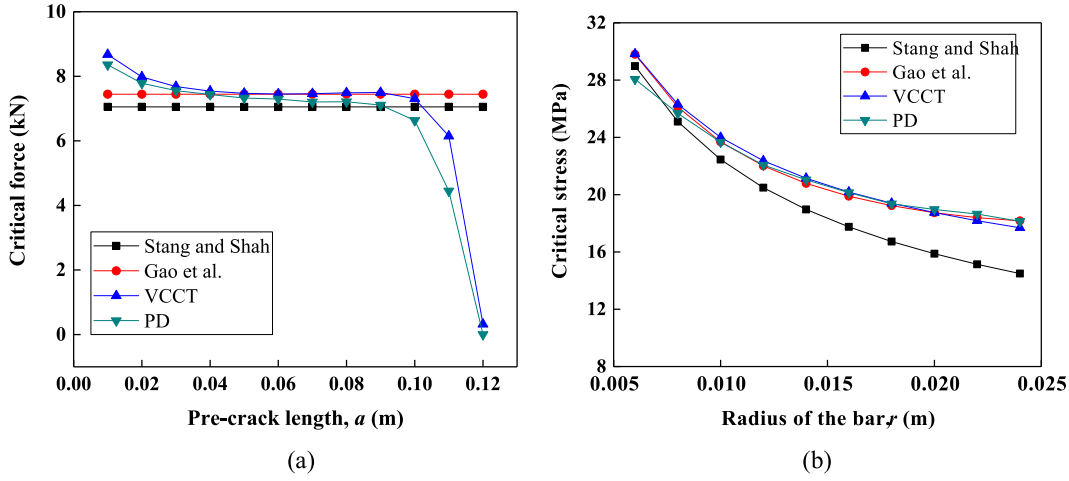

Fig. 14. Comparisons among different models: (a) critical force vs. pre-crack length, and (b) critical stress vs. radius of the bar.

where

$$k = \frac{c_1\nu_f + c_2\nu_m}{c_1(1-\nu_f) + 1 + \nu_m + 2c_2} \tag{33}$$

$$\eta = \frac{c_2(1-2k\nu_m)}{c_1(1-2k\nu_f)} \tag{34}$$

and $c_1 = E_m/E_f$, $c_2 = r^2/(R^2 - r^2)$. The critical forces predicted by both the theoretical models above are independent of the pre-crack length. Also, in Eqs. (31) and (32), the interfacial friction effect is not taken into consideration.

The PD results are compared not only with the VCCT model of FEM, but also with these two theoretical models in Eqs. (31) and (32). It can be found in Fig. 14(a) that the PD results agree well

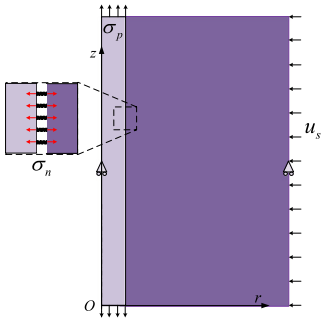

Fig. 15. Normal contact on the interface between the bar and the matrix.

with the VCCT results of FEM when the pre-crack is not close to the bottom of the bar. As shown in Fig. 14(b), almost all the PD results are in good agreements with those of VCCT and Gao et al. (1988)'s model. The results obtained by the model of Stang and Shah (1986) have large deviations from VCCT when the radius of the bar is large because their model ignores the effect of the volume fraction of the bar (Gao et al., 1988). The PD results have a maximum error compared to VCCT when the radius r is the smallest (see Fig. 14(b)). A small r and a fixed δ result in a large ratio of δ/r which thus increases the error as shown in Fig. 13(b).

4.3. Interfacial contact and friction

The normal contact and friction in the newly proposed PD contact model in Section 2.3 are related by the Coulomb's Law. Both the PD normal contact and the PD friction models are validated in the following.

4.3.1. Normal contact

To validate the normal contact part of PD modeling, a case study is considered, as shown in Fig. 15. A bar is embedded in the matrix, but it is divided by a pre-crack plane which goes across the whole interface, suggesting that the bar and the matrix are not bonded at all. The geometry in Fig. 15 are the same as those shown in Fig. 4. The shrinkage of the matrix is defined to be $\varepsilon_s = u_s/R$, and it is simulated by the direct applied radial displacement u_s on the outer surface of the matrix (Li and Mobasher, 1998). The axial stress σ_p is applied to both ends of the bar which will lead to the contraction of the bar in the radial direction, and it thus decreases the interfacial normal contact pressure σ_n. This is caused by the Poisson's contraction effect in the pull-out test.

A radial displacement $u_s = 8\times10^{-6}$ m is applied to the outer surface of the matrix by an increment $\Delta u_s = 4\times10^{-9}$ m every time step to simulate the shrinkage. The axial stress is set to be 0 in the cases where the Poisson's contraction is not of a concern.

The search interval C_n of the PD contact model is set to be 100 in all the following cases involving contact. The contact horizon δ_c is an extra parameter, and m_c is defined to be $\delta_c/\Delta x$ in the PD cases involving contact. In this study, the contact horizon δ_c must not be larger than the material horizon δ to avoid non-physical contact between particles belong to the same intact material body. The following three groups of discretization parameters are investigated and compared for the normal PD contact model.

- Group A: $m(\delta/\Delta x)$ and $m_c(\delta_c/\Delta x)$ are fixed as 3, and Δx is set as $r/20$, $r/30$, and $r/40$, which means equal m and m_c but varying δ and δ_c.
- Group B: δ and δ_c are fixed as $r/10$, and Δx is set as $r/20$, $r/30$, and $r/40$, which means equal δ and δ_c but varying m and m_c (2, 3, 4).
- Group C: m is fixed as 4, and δ is fixed as $r/10$. m_c is set as 2, 3, 4, which means equal m, m_c, and δ but varying δ_c.

As shown in Fig. 16, the total interfacial normal contact forces are evaluated during the shrinkage. The radial displacement u_s is applied by 2000 time steps. As demonstrated in Fig. 16, the fast responses are shown during the shrinkage, and the steady contact states are achieved by the contact model in all PD numerical cases. The normal contact pressures along the interface in the steady states are plotted in Fig. 17. The contact pressure in PD is transferred from the PD contact force density (Lehoucq and Silling, 2008). The PD results are compared with the FEM ones to quantitatively verify the contact model. As shown in Fig. 17, the contact pressures obtained by PD match well with those of FEM. The results obtained on the PD discretization of $m=4$ and $\Delta x = r/40$ show best agreements with FEM. The sharp derivations occurring at both ends of the bar may result from the absence of the intact half-circle contact region for the particles in the corners.

Average contact pressures induced by different matrix shrinkages are also evaluated. As shown in Fig. 18, the PD contact pressures increase linearly with the increase of shrinkage. The PD results keep good match with the FEM ones as demonstrated in Fig. 18. Consequently, the PD results using $m=4$ and $\Delta x = r/40$ show best agreements with FEM.

In addition, the Poisson's contraction effect in the PD contact model is investigated. As shown in Fig. 19, the matrix shrinkage ε_s is fixed as 1×10^{-4}, and the average PD contact pressures are evaluated under different axial pull stresses. As observed in Fig. 19, the average contact pressures decrease linearly with the increase of the pull stress σ_p. The PD results using $m=4$ and $\Delta x = r/40$ again agree best with FEM.

4.3.2. Friction sliding

The simulation case shown in Fig. 20 is computed for the verification of the friction part of PD contact modeling. All the interfacial bonding is still eliminated by the pre-crack between the bar and the matrix. A radial displacement $u_s = 8\times10^{-6}$ m is also applied to the outer surface of the matrix by an increment of $\Delta u_s = 4\times10^{-9}$ m every time step to generate the shrinkage strain of $\varepsilon_s = 1\times10^{-4}$. A very small axial displacement increment of $\Delta u = 1\times10^{-11}$ m is first applied to the top end of the bar until the axial displacement reaches $u = 5\times10^{-7}$ m. It will then achieve a steady initial pull-out friction state ($s \approx 0$). After that, the axial displacement u will increase to 0.08 m by an incremental $\Delta u = 8\times10^{-8}$ m to pull the bar out of the matrix. The friction stress will be induced during the pull-out process due to the matrix shrinkage if the interface has a non-zero friction coefficient f. The node size of the peridynamic discretization is $\Delta x = r/40$, the material horizon is $\delta = 4\Delta x$, and the contact horizon is $\delta_c = 3\Delta x$.

An analytical model is derived for quantitative comparisons with the PD results. As shown in Fig. 20, the bar is pulled out of the matrix at some time and the pull-out displacement is denoted as s in which the axial deformation of the bar is ignored. Considering the Poisson's contraction of the bar, the friction stress will be a function of the coordinate z and not be uniform along the contact interface. At an arbitrary location $z=l$, one has

$$\pi r^2 \sigma_p(l) = 2\pi r \int_0^l \sigma_f(z)dz \tag{35}$$

and the Coulomb's friction model states that

$$\sigma_f = f\sigma_n \tag{36}$$

The linear decrease of σ_n caused by σ_p due to the Poisson's contraction is expressed as

$$\sigma_n = \sigma_0 - K\sigma_p \tag{37}$$

where σ_0 is the normal contact pressure due to matrix shrinkage when $\sigma_p = 0$. Therefore, at the boundary $l=0$, the normal contact pressure is σ_0 and the friction stress is $\sigma_f = f\sigma_0$. Combining

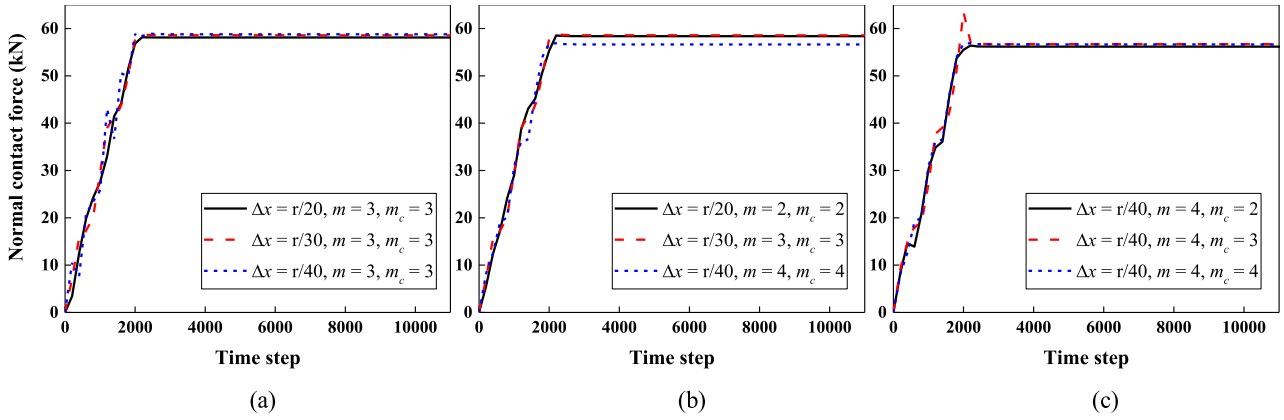

Fig. 16. Normal contact force during the shrinkage obtained by PD.

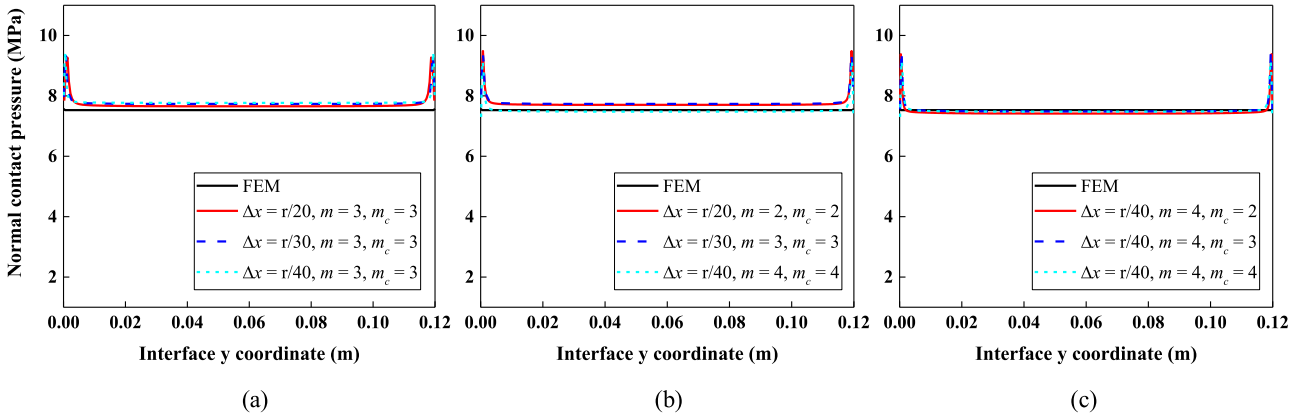

Fig. 17. Normal contact pressure distribution along the interface in steady contact state.

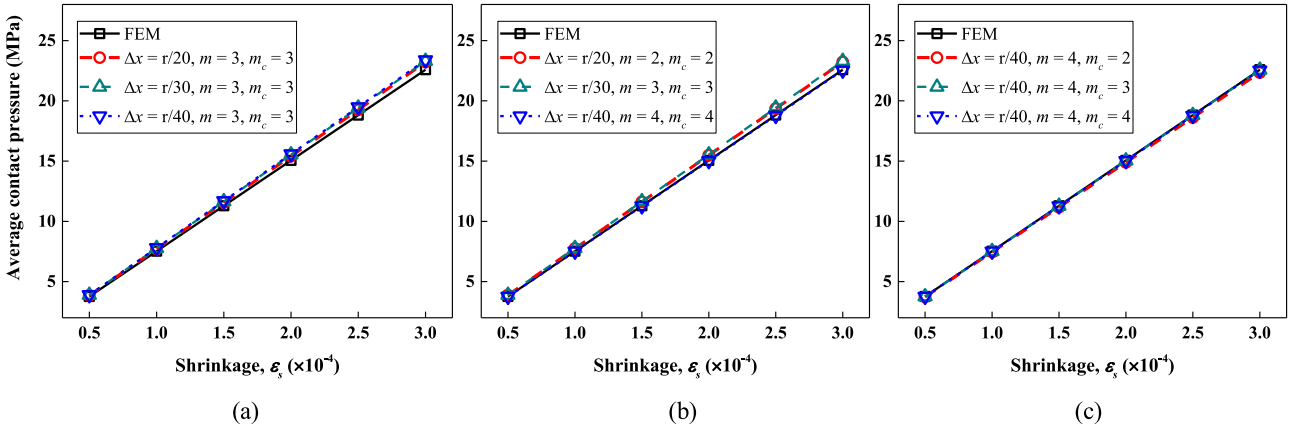

Fig. 18. Average contact pressure vs. matrix shrinkage.

Eqs. (35)-(37) and the boundary condition, one can solve that

$$\sigma_f(z) = f\sigma_0 e^{-2Kf\frac{z}{r}} \tag{38}$$

and the total friction force at this moment is

$$F_f = 2\pi r \int_0^{L-s} \sigma_f(z)dz = \frac{\pi r^2 \sigma_0}{K}\left(1 - e^{-2Kf\frac{L-s}{r}}\right) \tag{39}$$

In this friction part of PD contact model validation, the matrix shrinkage is fixed as $\varepsilon_s = 1 \times 10^{-4}$. σ_0 and K are determined by the FEM results in Section 4.3.1 to be 7.53 MPa and 0.044, respectively.

The distributions of the friction stresses along the interface in the initial pull-out state where $s \approx 0$ are shown in Fig. 21. The friction force density on the PD particles is transferred into the friction stresses of the classical theory on the contact surfaces. Three friction coefficients f (i.e., 0.2, 0.4 and 0.6) are used in Fig. 21 for both the analytical model and PD. It can be found that the PD results of different friction coefficients are in good agreements with the corresponding analytical results along the interface except for the regions near both ends. The total friction forces on the interface are further evaluated under different friction coefficients. The comparisons of the total friction forces with different friction coefficients between the PD simulation and the analytical model are plotted in Fig. 22. The PD predictions agree very well with the analytical solution. The maximum relative error of the PD total friction force

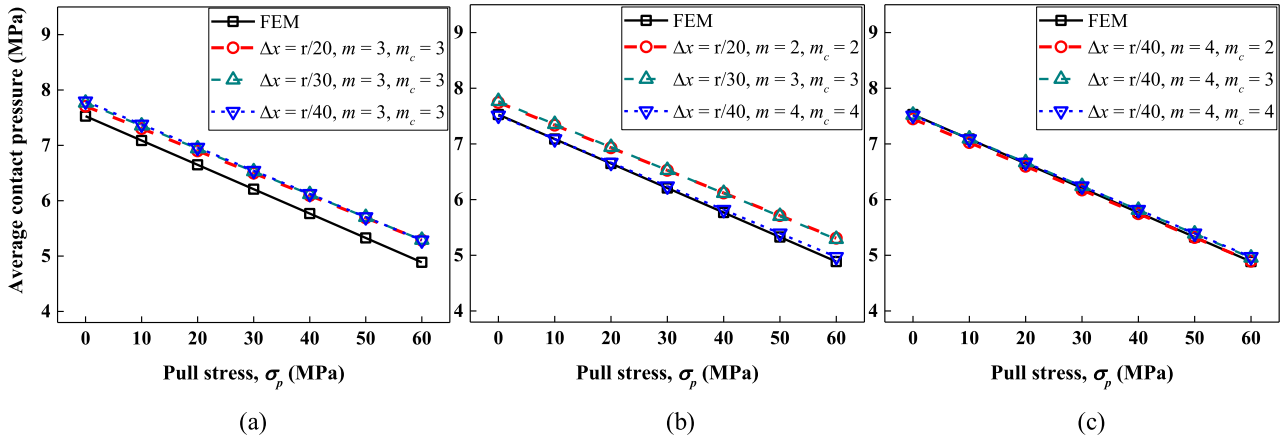

Fig. 19. Average contact pressure under different axial pull stresses.

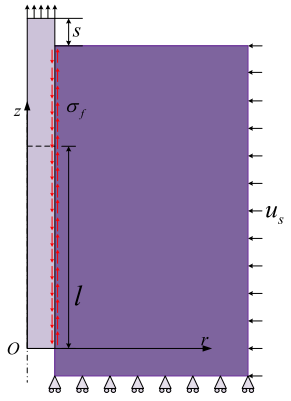

Fig. 20. Friction sliding during the pull-out of the bar.

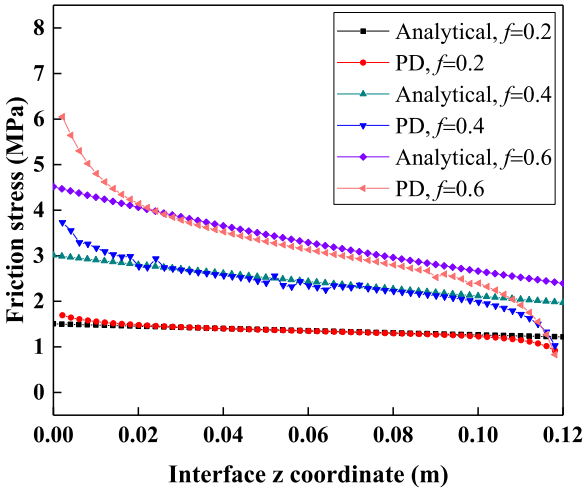

Fig. 21. Friction stress distribution along the interface in the initial pull-out friction state.

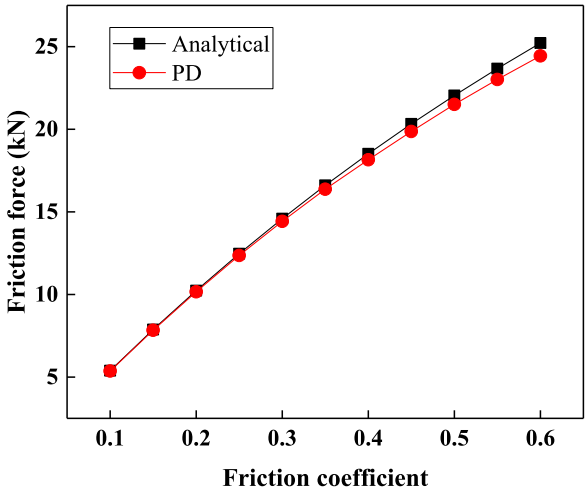

Fig. 22. Total friction force of different friction coefficients in the initial pull-out friction state.

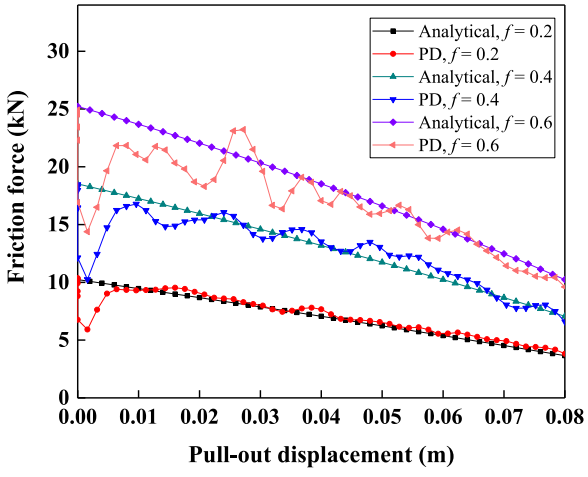

Fig. 23. Friction force during the pull-out of the bar.

results to the analytical solution is 3% when the friction coefficient is 0.6 (see Fig. 22).

The total friction force versus the pull-out displacement during the pull-out process are obtained by PD and the analytical model. The oscillation existing in the PD force curves obtained by the time integration solvers is reduced by the smoothness priors analysis (Kitagawa and Gersch, 1996) which is an effective trend extraction method for data series. Three friction coefficients of 0.2, 0.4, 0.6 are also used, and the results of both PD and the analytical model are compared in Fig. 23. As shown in Fig. 23, the PD results can keep a good match with the analytical ones. The PD curves show sudden drops in the early stage of the pull-out process which implies that the sudden jump of the displacement increment Δu from 1×10^{-11} m to 8×10^{-8} m every time step

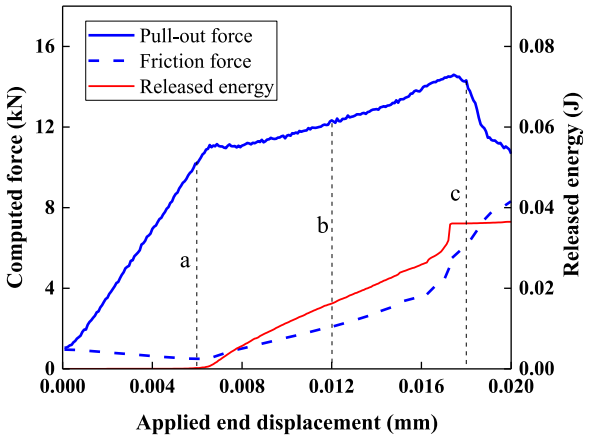

Fig. 24. The pull-out force, the friction force and the released energy during the pull-out process.

will break the steady contact state for a while. As also shown in Fig. 23, the PD results with a smaller friction coefficient show more stable behavior and better agreement with the analytical model.

4.4. Whole process of pull-out simulation

In addition to the individual validations of the three PD modeling parts above, the whole process of the pull-out is simulated. The geometric sizes and material properties used in Sections 4.1 are also used here for the whole process of pull-out simulation except that the pre-crack length $a = 10$ mm is set as the initial interface crack. Both the interfacial debonding and the friction sliding are considered. The critical energy release rate of interface (interfacial fracture toughness) and the friction coefficient of the interface are set to be $G_{ic} = 6$ J/m^2 and $f = 0.2$, respectively, in the first place. The node size of the peridynamic discretization is $\Delta x = r/40$, the material horizon is $\delta = 4\Delta x$, and the contact horizon is $\delta_c = 3\Delta x$.

In each beginning of the simulations, a radial displacement $u_s = 8 \times 10^{-6}$ m as shown in Figs. 15 and 20 is applied to the outer surface of the matrix by an increment of $\Delta u_s = 8 \times 10^{-10}$ m to simulate the matrix shrinkage. After that, the matrix shrinkage is held, and an axial displacement u is applied to the top end of the already-deformed bar by an increment of $\Delta u = 4 \times 10^{-10}$ m.

The pull-out force, friction force and released fracture energy are plotted in Fig. 24, with respect to the applied end displacement. The axial displacement, local damage, and friction force of the bar/matrix system at three situations (a, b, c) as indicated in Fig. 24 are further extracted in Fig. 25.

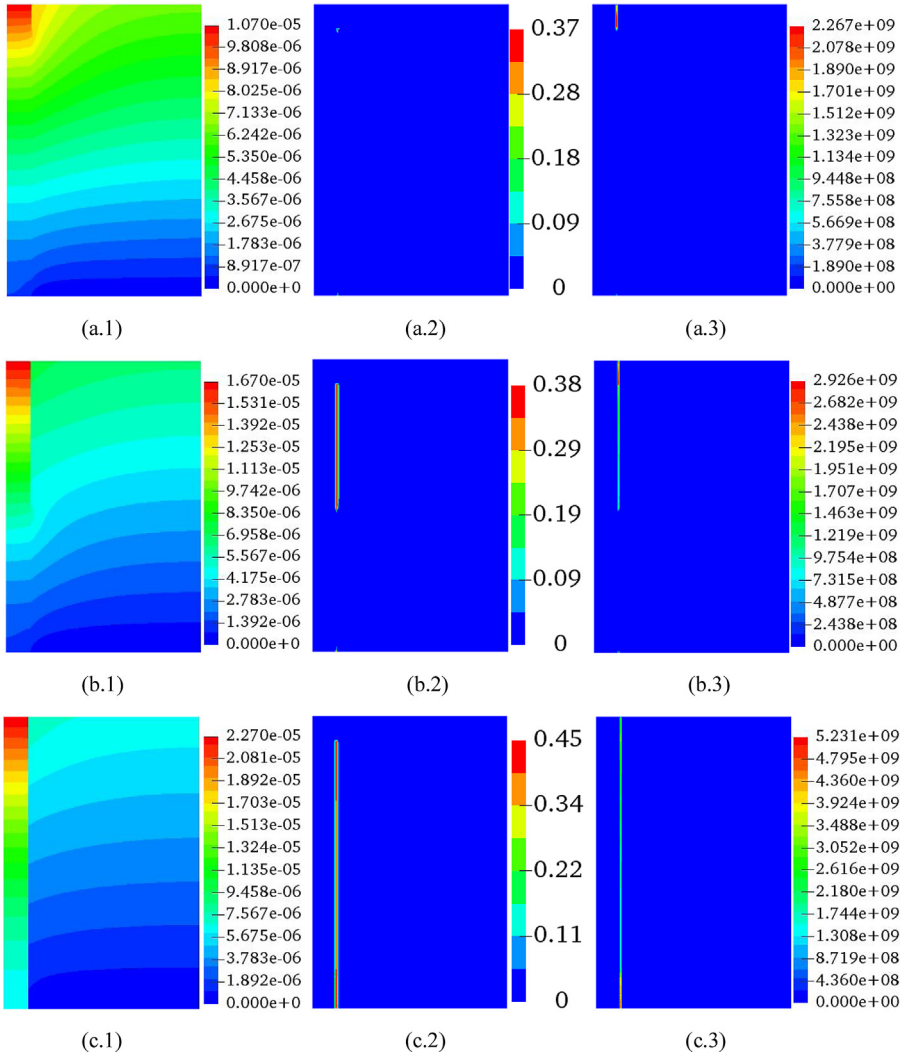

Fig. 25. The computed variable fields at three situations (a, b, c) (see Fig. 24) during the pull-out process: the axial displacement (a.1, b.1 and c.1), the local damage (a.2, b.2 and c.2), and the friction force density (a.3, b.3 and c.3).

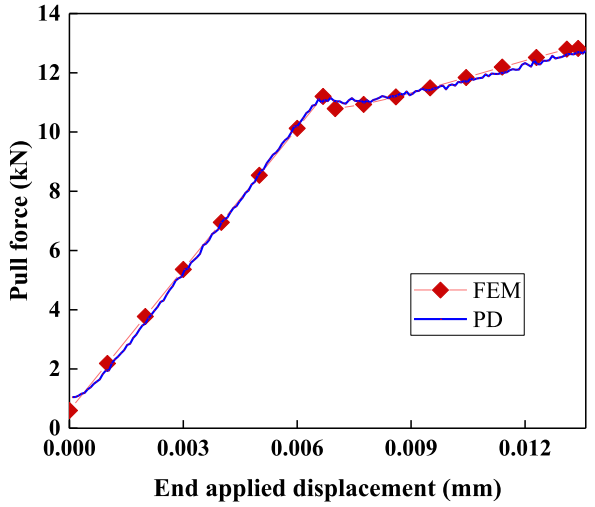

Fig. 26. The pull-out force vs. end applied displacement obtained by PD and FEM.

The axial displacement at the top end of the bar in Fig. 25 is the sum of the applied end displacement and the initial displacement caused by the matrix shrinkage. As shown in Figs. 24 and 25(a.1, a.2, and a.3), before the crack propagation, the friction force exists on the pre-crack surface and decreases due to the Poisson's contraction with the increase of the pull-out force. During the crack propagation and interfacial debonding, as shown in Figs. 24 and 25(b.1, b.2, and b.3), the interface energy is released and the newly-formed debonding surface participates in the interfacial friction, which will increase the friction force and further increase the pull-out force. When the crack propagates across the total interface, as shown in Figs. 24 and 25(c.1, c.2, and c.3), the pull-out force drops but the friction force still increases, which implies that the Poisson's contraction of the bar weakens. As shown in Fig. 25(b.1, b.2, and b.3), the maximum of the local damage value along the newly formed interfacial crack is 0.38, and it is smaller than the expected value 0.41 in the PD case of $m=4$, which means that some interfacial PD bonds are still unbroken even when the interface has already debonded. This kind of unbroken-bonds phenomenon was also found in the thermally-driven crack simulation by Xu et al. (2018). Considering that the applied shrinkage will increase the proportion of the mode II fracture component, it is deduced that the failure criterion based on the bond energy density has limitations in cases where the mode II fracture component dominates. The limitation of the bond energy density-based failure criterion on the mode II dominant fracture has also been recently observed by Zhang and Qiao (2019).

Some force-displacement results before and during interfacial debonding are obtained by FEM and compared with the PD ones in Fig. 26. The axisymmetric stress element, and the VCCT as well as the hard contact model are used together in ABAQUS for the FEM calculation. Considering the complexity of the whole process in the FEM simulation, FEM data is obtained not by one single continuous FEM simulation, rather than using several static FEM calculations with different successive interface debonding lengths as an equivalence to the quasi-static interface crack propagation. The related parameters considered in both PD and FEM calculations are same. As shown in Fig. 26, in spite of the limitations of the failure criterion discussed above, the critical force for the interfacial crack initiation predicted by PD still agrees well with the FEM one. However, as shown in Fig. 25(b.3), the remaining unbroken bonds mentioned above will result in insufficient contact on the newly-formed debonding surfaces and thus a loss of the friction forces. Therefore, the friction coefficient on the newly-formed debonding surface is modified by a reduction factor of 0.5 in the calculation of FEM for comparisons. As shown in Fig. 26, the FEM results after the correction keep a good match with the PD ones, which means that the insufficient contact issues in PD can be compensated by appropriately enhancing the friction coefficient on the newly-formed interfacial crack surface. The PD bond failure criteria which can avoid the unbroken-bonds issue in the mode II dominant fracture need further investigations, and the PD simulation for pull-out tests may be improved by the new PD bond failure criterion based on the critical skew recently proposed by Zhang and Qiao (2019).

The influences of friction coefficient and interfacial fracture toughness on the pull-out behavior are investigated. Two more cases with $f=0$ and 0.1 and a fixed $G_{ic}=6$ J/m^2 are simulated for the influence of the friction coefficient. In addition, two more cases with $G_{ic}=12$ J/m^2 and 24 J/m^2 and a fixed $f=0.2$ are also simulated for the effect of the interfacial fracture toughness. The force-displacement curves are plotted in Fig. 27. The discussion is focused on the stage involving both the interfacial debonding

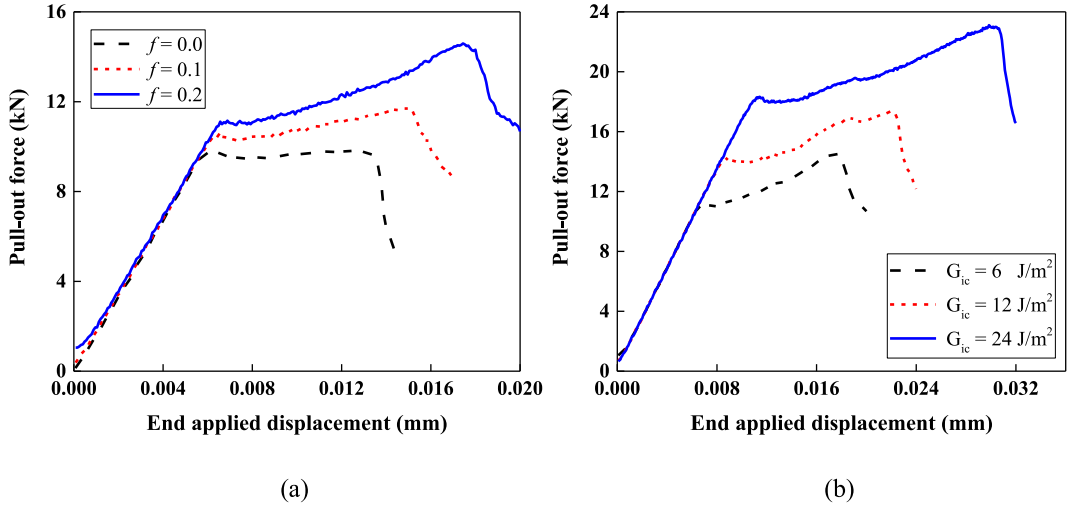

Fig. 27. The force-displacement curves of the pull-out processes: (a) different friction coefficients and a fixed interfacial fracture toughness, and (b) different interfacial fracture toughness values and a fixed friction coefficient.

and friction sliding. It can be found that the friction coefficient mainly influences the slope of the curve during interfacial debonding while the interfacial fracture toughness directly change the critical load when the interfacial crack starts to propagate.

As shown in Figs. 26 and 27, the developed peridynamic scheme involving three step-by-step modeling parts is capable of simulating the whole process of the pull-out tests continuously and spontaneously. The PD prediction capabilities (e.g., including the interface local damage, the interface released energy, and the interface friction force) can be obtained real-time during the simulation. The further comparative study between a more comprehensive PD pull-out simulation and the experiment is still ongoing. The research in progress is making efforts to (1) improve some aspects of the simulation framework, e.g., more realistic interfacial failure and contact models in the proposed scheme, and (2) conduct some experimental testing with sufficient parameter measurements for detailed comparisons and computational analysis. Furthermore, very small ratio of the fiber radius to the matrix radius must be treated using some PD local refinement techniques (Areias et al., 2018; Bobaru and Ha, 2011; Dipasquale et al., 2014; Ren et al., 2017, 2016; Shojaei et al., 2018; Silling et al., 2014) if the single fiber pull-out tests are simulated.

5. Conclusions

A systematic ordinary state-based peridynamic (OSBPD) scheme for the fiber/bar pull-out simulation in the 2D axisymmetric domain is developed. An axisymmetric PD model and a bond energy density failure criterion are used for analyzing the axisymmetric deformation and interfacial debonding, respectively. A new PD contact model is for the first time proposed for the friction sliding in the pull-out simulation, and a PD contact checking and computing algorithm is implemented in the meshfree PD codes for the contact model. The three individual modeling parts (i.e., the axisymmetric OSBPD model, failure criterion for interfacial debonding, and contact model) and whole pull-out process (i.e., combining the three modeling parts in a step-by-step fashion) in the PD pull-out simulation scheme are all quantitatively validated.

The axisymmetric PD model can capture the axisymmetric deformation accurately. The critical interfacial debonding loads predicted by the critical bond energy density failure criterion using a suitable PD discretization also agree very well with the ones obtained by the conventional VCCT in FEM and some analytical models. The convergence behaviors of both the axisymmetric PD model and the failure criterion for interfacial debonding are investigated based on the same set of PD discretization. It is found that the PD discretization has a pronounced influence on the errors of failure criterion than the deformation model.

The normal contact and friction sliding aspects of the proposed PD contact model are also verified numerically. Good quantitative agreements of the interfacial normal contact pressures obtained by the PD model and FEM under the same matrix shrinkage are achieved. The influences of the PD material horizon, the particle size and the PD contact horizon on the performance of the PD normal contact are also discussed. The ratio m shows the most obvious impact on the accuracy of the PD normal contact model. The friction aspect of the PD contact model is demonstrated by its comparisons with the analytical model considering the Poisson's contraction effect. The transferred friction stress distributions and the total friction forces using different friction coefficients during the pull-out process predicted by the PD contact model are in good agreement with the analytical solutions.

Finally, the whole process of the pull-out test is simulated continuously by the PD scheme considering the axisymmetric deformation, interfacial debonding, and friction sliding on the cracked surfaces. The unbroken-bond issue during the simulation and the corresponding correction are addressed and discussed, and an excellent agreement of bond-slip curves between the PD and FEM simulations is obtained. The influences of the interface friction coefficient and the interfacial fracture toughness on the bond-slip behavior in the pull-out simulation are investigated. The developed PD scheme for the fiber/bar pull-out simulation is capable of accurately simulating the deformation, interfacial debonding, and contact/friction during the pull-out process, and it can be further extended for bar/fiber push-out simulations.

Acknowledgment

The authors would like to acknowledge the partial financial support from the National Natural Science Foundation of China (NSFC Grant Nos. 51478265 and 51679136).

References

Areias, A., Reinoso, J., Camanho, P.P., César de Sá, J., Rabczuk, T., 2018. Effective 2D and 3D crack propagation with local mesh refinement and the screened Poisson equation. Eng. Fract. Mech. 189, 339–360.
Baena, M., Torres, L., Turon, A., Barris, C., 2009. Experimental study of bond behaviour between concrete and FRP bars using a pull-out test. Compos. Part B 40, 784–797.
Banholzer, B., Brameshuber, W., Jung, W., 2005. Analytical simulation of pull-out tests-the direct problem. Cem. Concr. Compos. 27, 93–101.
Beckert, W., Lauke, B., 1996. Finite element calculation of energy release rate for single-fibre pull-out test. Comput. Mater. Sci. 5, 1–11.
Beckert, W., Lauke, B., 1997. Critical discussion of the single-fibre pull-out test: does it measure adhesion? Compos. Sci. Technol. 57, 1689–1706.
Beglarigale, A., Yazici, H., 2015. Pull-out behavior of steel fiber embedded in flowable RPC and ordinary mortar. Constr. Build. Mater. 75, 255–265.
Benzeggagh, M.L., Kenane, M., 1996. Measurement of mixed-mode delamination fracture toughness of unidirectional glass/epoxy composites with mixed-mode bending apparatus. Compos. Sci. Technol. 56, 439–449.
Bobaru, F., Foster, J.T., Geubelle, P.H., Silling, S.A., 2016. Handbook of Peridynamic Modeling. Taylor & Francis.
Bobaru, F., Ha, Y.D., 2011. Adaptive refinement and multiscale modeling in 2D peridynamics. Int. J. Multisc. Comput. Eng. 9, 635–660.
Bobaru, F., Yang, M., Alves, L.F., Silling, S.A., Askari, E., Xu, J., 2009. Convergence, adaptive refinement, and scaling in 1D peridynamics. Int. J. Numer. Methods Eng. 77, 852–877.
Bobaru, F., Zhang, G., 2015. Why do cracks branch? A peridynamic investigation of dynamic brittle fracture. Int. J. Fract. 196, 59–98.
Camanho, P., Dávila, C., de Moura, M., 2003. Numerical simulation of mixed–mode progressive delamination in composite materials. J. Compos. Mater. 37, 1415–1424.
Chowdhury, S.C., Okabe, T., 2007. Computer simulation of carbon nanotube pull-out from polymer by the molecular dynamics method. Compos. Part A 38, 747–754.
Cosenza, E., Manfredi, G., Realfonzo, R., 1997. Behavior and modeling of bond of FRP rebars to concrete. J. Compos. Constr. 1, 40–51.
Cunha, V.M.C.F., Barros, J.A.O., Sena-Cruz, J.M., 2010. Pullout behavior of steel fibers in self-compacting concrete. J. Mater. Civil Eng. 22, 1–9.
Delfolie, C., Depecker, C., Lefebvre, J.M., 1999. Interfacial phenomena in glass fibre reinforced polyester resin with low profile additives. J. Mater. Sci. 34, 481–495.
DiFrancia, C., Ward, T.C., Claus, R.O., 1996. The single-fibre pull-out test. 1: Review and interpretation. Compos. Part A 27, 597–612.
Dipasquale, D., Zaccariotto, M., Galvanetto, U., 2014. Crack propagation with adaptive grid refinement in 2D peridynamics. Int. J. Fract. 190, 1–22.
Dubinsky, A., Elperin, T., 2015. Peridynamics analysis of the nanoscale friction and wear properties of amorphous carbon thin films. J. Mech. Mater. Struct. 10, 559–572.
Ellis, B.D., McDowell, D.L., Zhou, M., 2014. Simulation of single fiber pullout response with account of fiber morphology. Cem. Concr. Compos. 48, 42–52.
Fang, C., Lundgren, K., Plos, M., Gylltoft, K., 2006. Bond behaviour of corroded reinforcing steel bars in concrete. Cem. Concr. Res. 36, 1931–1938.
Foster, J.T., Silling, S.A., Chen, W., 2011. An energy based failure criterion for use with peridynamic states. J. Multisc. Comput. Eng. 9, 675–687.
Gao, Y.C., Mai, Y.W., Cotterell, B., 1988. Fracture of fiber-reinforced materials. J. Appl. Math. Phys. 39, 550–572.
Ha, Y.D., Bobaru, F., 2010. Studies of dynamic crack propagation and crack branching with peridynamics. Int. J. Fract. 162, 229–244.
Kang, J., Kim, K., Lim, Y.M., Bolander, J.E., 2014. Modeling of fiber-reinforced cement composites: discrete representation of fiber pullout. Int. J. Solids Struct. 51, 1970–1979.
Kilic, B., Agwai, A., Madenci, E., 2009. Peridynamic theory for progressive damage prediction in center-cracked composite laminates. Compos. Struct. 90, 141–151.
Kilic, B., Madenci, E., 2010. An adaptive dynamic relaxation method for quasi-static simulations using the peridynamic theory. Theor. Appl. Fract. Mech. 53, 194–204.

Kitagawa, G., Gersch, W., 1996. Smoothness Priors Analysis of Time Series. Smoothness Priors Analysis of Time Series. Springer.
Larralde, J., Silva-Rodriguez, R., 1993. Bond and slip of FRP rebers in concrete. J. Mater. Civil Eng. 5, 30–40.
Le, Q.V., Chan, W.K., Schwartz, J., 2014. A two-dimensional ordinary, state-based peridynamic model for linearly elastic solids. Int. J. Numer. Methods Eng. 98, 547–561.
Lehoucq, R.B., Silling, S.A., 2008. Force flux and the peridynamic stress tensor. J. Mech. Phys. Solids 56, 1566–1577.
Li, C.Y., Mobasher, B., 1998. Finite element simulations of fiber pull-out toughening in fiber reinforced cement based composites. Adv. Cem. Based Mater. 7, 123–132.
Li, Y., Liu, Y., Peng, X., Yan, C., Liu, S., Hu, N., 2011. Pull-out simulations on interfacial properties of carbon nanotube-reinforced polymer nanocomposites. Comput. Mater. Sci. 50, 1854–1860.
Lin, G., Geubelle, P.H., Sottos, N.R., 2001. Simulation of fiber debonding with friction in a model composite pushout test. Int. J. Solids Struct. 38, 8547–8562.
Littlewood, D.J., 2015. Roadmap for Peridynamic Software Implementation. Sandia National Laboratories Tech. Report SAND2015-9013.
Littlewood, D.J., 2010. Simulation of dynamic fracture using peridynamics, finite element modeling, and contact. In: Proceedings of the ASME 2010 International Mechanical Engineering Congress & Exposition. Vancouver, British Columbia, Canada, .
Lu, J., Zhang, Y., Muhammad, H., Chen, Z., 2018. Peridynamic model for the numerical simulation of anchor bolt pullout in concrete. Math. Probl. Eng. 2018, 1–10.
Parks, M.L., Littlewood, D.J., Mitchell, J.A., Silling, S.A., 2012. Peridigm Users' Guide. Sandia National Laboratories Tech. Report SAND2012-7800.
Penn, L.S., Chou, R.C.T., Wang, A.S.D., Binienda, W.K., 1989. The effect of matrix shrinkage on damage accumulation in composites. J. Compos. Mater. 23, 570–586.
Pochiraju, K.V., Tandon, G.P., Pagano, N.J., 2001. Analyses of single fiber pushout considering interfacial friction and adhesion. J. Mech. Phys. Solids 49, 2307–2338.
Popov, L.V., 2010. Contact Mechanics and Friction:Physical Principles and Applications. Springer.
Povirk, G.L., Needleman, A., 1993. Finite element simulations of fiber pull-out. J. Eng. Mater. Technol. 115, 286–291.
Qian, D., Dickey, E.C., Andrews, R., Rantell, T., 2000. Load transfer and deformation mechanisms in carbon nanotube-polystyrene composites. Appl. Phys. Lett. 76, 2868–2870.
Rabczuk, T., Ren, H., 2017. A peridynamics formulation for quasi-static fracture and contact in rock. Eng. Geol. 225, 42–48.
Ren, H., Zhuang, X., Cai, Y., Rabczuk, T., 2016. Dual-horizon peridynamics. Int. J. Numer. Methods Eng. 1885–1891.
Ren, H., Zhuang, X., Rabczuk, T., 2017. Dual-horizon peridynamics: a stable solution to varying horizons. Comput. Methods Appl. Mech. Eng. 318, 762–782.
Shannag, M.J., Brincker, R., Hansen, W., 1997. Pullout behavior of steel fibers from cement-based composites. Cem. Concr. Res. 27, 925–936.
Shojaei, A., Mossaiby, F., Zaccariotto, M., Galvanetto, U., 2018. An adaptive multi–grid peridynamic method for dynamic fracture analysis. Int. J. Mech. Sci. 144, 600–617.
Silling, S.A., 2000. Reformulation of elasticity theory for discontinuities and long-range forces. J. Mech. Phys. Solids 48, 175–209.
Silling, S.A., Askari, E., 2005. A meshfree method based on the peridynamic model of solid mechanics. Comput. Struct. 83, 1526–1535.
Silling, S.A., Epton, M., Weckner, O., Xu, J., Askari, E., 2007. Peridynamic states and constitutive modeling. J. Elast. 88, 151–184.
Silling, S.A., Lehoucq, R.B., 2010. Peridynamic theory of solid mechanics. Adv. Appl. Mech. 44, 73–168.
Silling, S.A., Littlewood, D.J., Seleson, P.D., 2014. Variable Horizon in a Peridynamic Medium. Sandia National Laboratories Tech. Report SAND2014-19088x.
Singh, S., Shukla, A., Brown, R., 2004. Pullout behavior of polypropylene fibers from cementitious matrix. Cem. Concr. Res. 34, 1919–1925.
Stang, H., Shah, S.P., 1986. Failure of fibre-reinforced composites by pull-out fracture. J. Mater. Sci. 21, 953–957.
Takaku, A., Arridge, R.G.C., 1973. The effect of interfacial radial and shear stress on fiber pull-out in composite materials. J. Phys. D 6, 2038–2047.
Torre-Casanova, A., Jason, L., Davenne, L., Pinelli, X., 2013. Confinement effects on the steel-concrete bond strength and pull-out failure. Eng. Fract. Mech. 97, 92–104.
Tsai, J., Patra, A.K., Wetherhold, R., 2003. Numerical simulations of fracture-toughness improvement using short shaped head ductile fibers. Compos. Part A 34, 1255–1264.
Tsai, J.H., Patra, A., Wetherhold, R., 2005. Finite element simulation of shaped ductile fiber pullout using a mixed cohesive zone/friction interface model. Compos. Part A 36, 827–838.
Wu, E., Reuter Jr, R.C., 1965. Crack Extension in Fiberglass Reinforced Plastics. University of Illinois T.& AM Report No. 275.
Xu, J., Askari, A., Weckner, O., Silling, S., 2008. Peridynamic analysis of impact damage in composite laminates. J. Aerosp. Eng. 21, 187–194.
Xu, Z., Zhang, G., Chen, Z., Bobaru, F., 2018. Elastic vortices and thermally-driven cracks in brittle materials with peridynamics. Int. J. Fract. 209, 203–222.
Yang, L., Tong, L., He, X., 2012. MD simulation of carbon nanotube pullout behavior and its use in determining mode I delamination toughness. Comput. Mater. Sci. 55, 356–364.
Ye, L.Y., Wang, C., Chang, X., Zhang, H.Y., 2017. Propeller-ice contact modeling with peridynamics. Ocean Eng. 139, 54–64.
Zhang, H., Qiao, P., 2018a. An extended state-based peridynamic model for damage growth prediction of bimaterial structures under thermomechanical loading. Eng. Fract. Mech. 189, 81–97.
Zhang, H., Qiao, P., 2018b. A state-based peridynamic model for quantitative fracture analysis. Int. J. Fract. 211, 217–235.
Zhang, Y., Qiao, P., 2018c. An axisymmetric ordinary state-based peridynamic model for linear elastic solids. Comput. Methods Appl. Mech. Eng. 341, 517–550.
Zhang, Y., Qiao, P., 2019. A new bond failure criterion for ordinary state-based peridynamic mode II fracture analysis. Int. J. Fract. 215, 105–128.
Zhou, L.-M., Kim, J.-K., Mai, Y.-W., 1993. Micromechanical characterisation of fiber/matrix interfaces. Compos. Sci. Technol. 48, 227–236.
Zhou, L.-M., Kim, J.-K., Mai, Y.-W., 1992. Interfacial debonding and fibre pull-out stresses - Part II A new model based on the fracture mechanics approach. J. Mater. Sci. 27, 3155–3166.
Zhou, X., Wang, Y., Xu, X., 2016. Numerical simulation of initiation, propagation and coalescence of cracks using the non-ordinary state-based peridynamics. Int. J. Fract. 201, 213–234.
Zhou, Z., Qiao, P., 2018. Bond behavior of epoxy-coated rebar in ultra-high performance concrete. Const. Build. Mater. 182, 406–417.